Application of a Design Optimization Strategy to Multi-Stage Compressor Matching

by

Jérôme Bert

Diplôme d'Ingénieur, Ecole Centrale Paris, 2005

Submitted to the Department of Aeronautics and Astronautics in
partial fulfillment of the requirements for the degree of

MASTER OF SCIENCE IN AERONAUTICS AND ASTRONAUTICS

at the

MASSACHUSETTS INSTITUTE OF TECHNOLOGY

February 2006

© 2006 Massachusetts Institute of Technology. All rights reserved.

MASSACHUSETTS INSTITUTE OF TECHNOLOGY
JUL 10 2006
LIBRARIES

Author .....
Department of Aeronautics and Astronautics
February 3, 2006

ARCHIVES

Certified by .....
Professor Zoltán S. Spakovszky
C. S. Draper Associate Professor of Aeronautics and Astronautics
Thesis Supervisor

Accepted by .....
Jaime Peraire
Professor of Aeronautics and Astronautics
Chair, Committee on Graduate Students

Application of a Design Optimization Strategy to Multi-Stage Compressor Matching

by

Jérôme Bert

Submitted to the Department of Aeronautics and Astronautics on February 3, 2006,
in partial fulfilment of the requirements for the degree of
Master of Science in Aeronautics and Astronautics

Abstract

A major challenge in the design of multi-stage compressors is the matching of stages to enable stable operation over a large range of mass flows and operating conditions. Particularly in turbofan low-pressure compressors, where a variable geometry cannot be implemented, design strategies for maximum efficiency at high speed can compromise the surge margin at low speed. In this thesis, a design optimization framework has been implemented to an industry-strength compressor-matching problem. The optimization framework combines a mean-line flow solver and a dynamic stability analysis of a six-stage low-pressure compressor of a modern turbofan engine to optimize the blade row geometry for enhanced stability at flight idle conditions. To assess the potential improvements in compressor stability at low speed, a number of optimization strategies are employed using different objective functions and stability metrics.

To estimate the performance and stability of the six-stage compressor, a mean-line flow solver is developed and coupled with a previously developed dynamic compressor-stability analysis. A fan-root flow model and an endwall loss correlation are developed using performance data provided by industry. The analysis reveals that the models enable an adequate estimation of the datum compressor performance. This methodology is then used in an optimization effort searching for the optimum compressor design.

A compressor blade parametrization based on Bezier splines is developed to explore a range of possible blade geometries. A CFD-based blade-row performance database is established using the blade-to-blade solver MISES. This facilitates an effective means to predict the blade performance for various geometries defined by the optimizer.

To find the best solution for the compressor-matching problem, a number of optimization strategies are applied to the datum compressor. The best result is obtained using an optimization strategy based on industry surge margin. An improvement of 14.8% in flight idle surge margin is achieved while maintaining the design pressure ratio and efficiency at climb speed within 1% and 0.3 points of the design values respectively. A compressor design optimization based on a dynamic-stability metric is also employed. Due to time constraints, this strategy could not be fully explored and the preliminary results suggest that further work is required.

The best results is a 14.8% improvement in the flight idle surge margin, but the re-matching of the compressor and the associated increase in the rotor loading of the second stage entail high-risk design modifications. This suggests that, given these design limitations, the best matching is achieved by the datum configuration. In summary, the thesis demonstrates that the developed compressor design optimization methodology is applicable to industry-strength design problems, and the framework is shown to have the potential to investigate compressor designs for optimum matching.

Thesis Supervisor: Professor Zoltán Spakovszky
Title: C.R. Draper Associate Professor of Aeronautics and Astronautics

Acknowledgement

I first wish to thank my advisor, Professor Spakovszky, for his guidance throughout the course of this research, his constructive comments, invaluable advice and most importantly, for having transformed this project into a great learning experience.

I wish to thank Lisa Brilliant and Kate Colson for their helpful emails and for running MISES calculations, Yuan Dong, Gavin Hendricks, Becky Rose, Tom Rogers, and Stanley Balamucky for their support and expertise, and for all the productive meetings we had at Pratt & Whitney.

I am grateful to François and Alfonso for all the hours spent in their office, for the crappy-food-lunch-time ritual at the student center, and simply for their friendship. I would like to thank Vai-Man for all the conversations we shared, Juan for explaining me his matlab codes, and also all the GTL students for the unforgettable social hours. I also wish to thank Theo.

Of course, I would like to thank my parents who played the largest role in giving me the opportunity to attend MIT in the first place and for their support and numerous encouragements over the last year and a half.

At last, I would like to thank Elise. Thank you for each time you came to Boston, for every minute we spent on the phone, and for much more...

This work was funded by Pratt & Whitney, Technical Monitor Dr. Yuan Dong.
This support is gratefully acknowledged.

Contents

Abstract 3

Acknowledgement 5

Contents 7

List of Figures 10

List of Tables 14

Nomenclature 15

1 Introduction 19

1.1 Technical Background 19

1.1.1 Compressor Matching 19

1.1.2 Compressor Stability 22

1.2 Previous Work 26

1.2.1 Stall Inception and Active Control 26

1.2.2 Dynamic Stability Metric 26

1.2.3 Generic 3-Stage Compressor Design Optimization 29

1.3 Nature of the Issue 30

1.4 Scope of the Thesis 31

1.4.1 Goals 31

1.4.2 Research Questions 31

1.4.3 Technical Roadmap 32

1.4.4 Outline of the Thesis 35

2 Datum Compressor Performance and Stability Estimation 36

2.1 Compressor Performance Estimation 36

2.1.1 Overview 36
2.1.2 Fan Root Model Description 38
2.1.3 Compressor Performance Estimation at Design Conditions 39
2.1.4 Off-Design Performance Estimation 41
2.2 Compressor Stability Estimation 43
2.2.1 Dynamic Stability Compressor Model 43
2.2.2 Stall Line Estimation 47

3 CFD Based Blade Performance Database **49**
3.1 Nature of the Issue 49
3.2 Parametric Description of Blade Profiles 50
3.2.1 Blade-Profile Parametrization 50
3.2.2 Thickness Distribution 52
3.2.3 Assessment of Blade Profile Parametrization 54
3.3 Database 55
3.3.1 Optimization Parameter Choice 55
3.3.2 Optimization Parameter Range 55
3.3.3 Database Generation 57

4 Datum Compressor Performance **58**
4.1 Implementation of Compressor Performance Estimation Method 58
4.2 Datum Compressor Performance Estimation 61
4.3 Datum Compressor Matching 64

5 Implementation of the Optimization Framework **68**
5.1 Optimization Strategy 68
5.1.1 Optimizer Settings 68
5.1.2 Assessment Metrics 69
5.2 Limitations of the Optimization Framework 70

5.2.1 Interpolation within the Blade Performance Database 70
5.2.2 Uncertainty Analysis 71

6 Compressor Design Optimization **76**

6.1 Optimization Result Using a SM_{ind} Based Objective Function 76
6.1.1 Optimization Strategy 76
6.1.2 Compressor Performance Optimization Results 77
6.1.3 Analysis of the Results 80
6.1.4 Compressor Design Implications 86
6.1.5 Discussion of Results 87
6.2 Optimization Result Using an S_d Based Objective Function 88
6.2.1 Setup of the Optimizer 88
6.2.2 Preliminary Results 89
6.2.3 Discussion of Results 91

7 Summary and Conclusions **92**

7.1 Compressor Performance Estimation 92
7.2 Blade Performance Prediction 93
7.3 Compressor Design Optimization Results 94
7.4 Recommendation for Future Work 95

Bibliography **96**

List of Figures

1.1 Velocity triangles for the front and back-end stages at design condition (dotted line) and at low speed (solid line). (Kerrebrock[9]) 20

1.2 Two early high-pressure ratio, multi-stage compressors and their characteristics. 21

1.3 Types of compressor instabilities: a. surge: low-frequency average mass flow oscillations and b. rotation stall: local mass flow variations with rotating wave structures 22

1.4 Compressor static stability: Point A is statically stable; point B is statically unstable 23

1.5 Two compressors with the same growth rate of flow-field perturbations at point 1 but with different robustness (adopted from Castiella [1]) 27

1.6 Compressor maps of compressors A and B (adopted from Castiella[1]) 28

1.7 S_d versus SM_{NASA} for compressors A and B of figure 1.6 (adopted from Castiella [1]) 29

1.8 Optimization Framework 33

2.1 Sketch of the gas-path geometry of the 6-stage low-pressure compressor investigated 37

2.2 Low pressure compressor blade rows 37

2.3 "3D/2D" loss coefficient description 41

2.4 The low-pressure compressor is divided into three distinct compressor blocks 42

2.5 Speed line adjustment: The blue speed line is modified to match the industry data in red (this is a sketch and is not to scale). 42

2.6 Representation of the compressor in the dynamic stability model 44

2.7 Eigenvalues of the harmonics 1, 2, and 3 for operating points at mass flow larger than the mass flow at surge point at design speed. 48

3.1 Blade profile parametrization 51

3.2 Definition of the blade metal angles and flow angles used. 52

3.3 Blade-profile parametrization: thickness distribution composed by four Bezier segments. (Figure not to scale) 53
3.4 Blade-profile parametrization: comparison between datum-blade profile (in red) and parameterized-blade profile (in blue). The two contours are superimposed. 54
3.5 Comparison between computed (MISES) loss buckets of the parameterized-blade profile (in blue) and loss buckets of the datum-blade profile (in red). The two loss buckets compare well, and the blade parametrization is assessed. Loss is expressed in terms of loss coefficient versus flow angle. 55
3.6 Effects of a 4° variation in stagger angle (a) and camber angle (b) on loss buckets. On both plots, the blue bucket corresponds to the lower value of blade angle, and the red bucket corresponds to the higher value of blade angle. 56
4.1 Blockage at each compressor axial location from Stator 1 trailing edge to Stator 6 trailing edge. 59
4.2 Corrections (in degrees) added to the blade-row deviation angles for different rotor speeds. 59
4.3 "3D/2D" loss coefficients applied to the blade-row 2D losses for different rotor speeds 60
4.4 Baseline compressor map. The performance estimation is plotted in blue; the performance measurements are plotted in red. The measured operating line is plotted as the black dashed line. 61
4.5 Compressor efficiency map. The performance estimation is plotted in blue; the performance measurement is plotted in red. 62
4.6 Blade-row loss buckets of the datum compressor at design speed. From left to right are plotted the surge point (denoted SP), the design point (denoted OP), and a point on the choke side of the compressor characteristic (denoted CP). 65

4.7 Blade-row loss buckets of the datum compressor at flight idle conditions. From left to right are plotted the surge point (denoted SP), the design point (denoted OP), and a point on the choke side of the compressor characteristic (denoted CP). 66

5.1 The low-speed surge margin versus Rotor 2 geometry (stagger and camber angles). Other blade rows are kept at their baseline geometries. 72

5.2 Variations of Rotor 2 geometry (stagger and camber angles) during one complete optimization. The full 2° parameter ranges for these angles have not been explored. 74

6.1 Comparison between the optimized-compressor map (SM_{ind} optimization) and the datum-compressor map 78

6.2 Comparison between the optimized-compressor map (SM_{ind} optimization) and the datum-compressor map (low-speed enlarged view) 78

6.3 Comparison between the optimized-compressor efficiency map (SM_{ind} optimization) and the datum-compressor efficiency map. 79

6.4 a) Variation of blade stagger angles and b) variation of blade camber angles between the optimized-compressor blades and the datum-compressor blades . 80

6.5 SM_{ind}-based optimization: blade-row loss buckets at low speed surge point for the datum compressor (in blue) and the optimized compressor (in red). The solid-red line corresponds to the loss buckets interpolated using the database; the dashed-red line corresponds to loss buckets computed by MISES. 81

6.6 Changes in the incidence angles (a) and the flow angles (b) between the datum compressor and the optimized compressor for the SM_{ind}-based optimization. 83

6.7 Blade-row loss buckets at the design speed operating point for the datum compressor (in blue) and the optimized compressor (in red) (SM_{ind}-based optimization). The solid-red line corresponds to loss buckets from the database; the dashed-red line corresponds to loss buckets MISES provides. 85

6.8 a) Variation of the diffusion factor of the blade rows and b) variation of the work coefficient of the rotor blade rows at the design-speed operating point. . 86

6.9 S_d-based optimization: comparison between the resulting-compressor map and datum-compressor map (low-speed enlarged view). 91

List of Tables

4.1 Compressor-performance comparison between estimation and measurement . 63

4.2 Surge-margin comparison between estimation and measurement 63

5.1 Blade row loss for three Rotor 2 geometries 73

6.1 Constraints used in the SM_{ind}-based optimization 77

6.2 Comparison between optimized-compressor performance and datum-compressor performance on the operating line for the SM_{ind}-based optimization. 77

6.3 Changes in the flow angles, the inlet blade metal angles and the incidence angles between the datum compressor and the optimized compressor for an SM_{ind}-based optimization. 82

6.4 Constraints used in the S_d-based compressor design optimization. 89

6.5 S_d-based optimization: changes in blade angles between the resulting compressor and the datum compressor. The changes are negligible. 90

6.6 S_d-based optimization: comparison between output-compressor performance and datum-compressor performance on the operating line. 90

Nomenclature

Acronyms

CFD	Computational Fluid Dynamics
CP	Choke Point: operating point on the choke side of the compressor characteristic
DF	Diffusion Factors
EC	Exit Conditions
IC	Initial Conditions
LPC	Low Pressure Compressor
MG	Moore-Greitzer
MIT	Massachusetts Institute of Technology
OP	Operating Point
PR	Pressure Ratio
SM	Surge Margin
SP	Surge Point
SQP	Sequential Quadratic Programming

Greek

α	Absolute flow angle
β	Relative flow angle
$\beta*$	Blade metal angle
γ	Stagger angle
Δ	Finite variation
δ	Deviation angle, correction to deviation angle, variable increment
θ	Angular coordinate in the cylindrical frame, camber angle
κ	Unstaggered blade metal angle

λ	Blade passage inertia
μ	Stator blade row inertia
π	Pressure ratio
σ	Growth rate of the flow field perturbations, solidity
τ	Unsteady loss time lag
ϕ	Flow coefficient
ψ	Pressure rise coefficient
ω	Rotation rate of the flow field perturbations

Roman

AR	Blade row area-density ratio
b	Baseline blade parameter value
B	Transmission matrix
c_x	Axial chord
det	Determinant
i	Index
j	Complex number
k_t	Throttle coefficient
L	Loss coefficient
$\dot{m}$	Mass flow
M	Number of discreet point on the compressor characteristic
n	harmonic number, integer
Nstage	Number of stage
P	Pressure
p	Blade parameter
r	Radius

R	Robustness, rotor blade row
s	Laplace variable, eigenvalue
S	Stator blade row
S_d	Dynamic stability metric
t_m	Maximum blade thickness
T	Temperature, transmission matrix
U	Wheel speed
V	Flow velocity
x_m	Location of maximum blade thickness
w	Weight distribution

Superscripts

$\sim$	Linearized quantity
$\bar{}$	Mean quantity
$'$	Quantity evaluated in the relative frame
$datum$	Relative to the datum compressor
TS	Total-to-static
SS	Steady-state

Subscripts

1	Upstream
2	Downstream
$corr$	Corrected quantity
I	Isentropic
ind	Industrial, defined by industry

ini	Initial, baseline quantity
$operating$	At operating point
NASA	Defined by NASA
R	Rotor
ref	Reference
rot	Rotor
S	Stator
$speed$	Rotor speed
sta	Stator
$surge$	At surge point
sys	System
T	Stagnation quantity
x	In meridional direction
θ	In tangential direction

Chapter 1

Introduction

1.1 Technical Background

1.1.1 Compressor Matching

Compressors are generally designed to maximize pressure ratio and efficiency at design conditions, or cruise conditions, since the engine operates there during most of its mission. However, at other flight conditions compressors still need to meet off-design performance and operability requirements. High-pressure ratio, multi-stage compressors in aircraft engine have some difficulties achieving operability requirements at these off-design operating conditions (Kerrebrock [9]).

At design conditions, the compressor geometry is designed to meet the pressure ratio and efficiency requirements. For a constant flow coefficient throughout the compressor, the gas-path cross-section area needs to be reduced as pressure builds up through the machine and the flow density increases. The flow-path area at every stage of the machine is thus set by design conditions and design-performance requirements.

At flight idle conditions, the rotor speed is about 40% of the design speed, and the mass flow through the compressor is much less than the design mass flow, so the reduction in the flow-path area is no longer correct. For the front-end stages, since mass flow is low and the flow-path area is large, flow coefficient is low and incidence angles on the blade rows

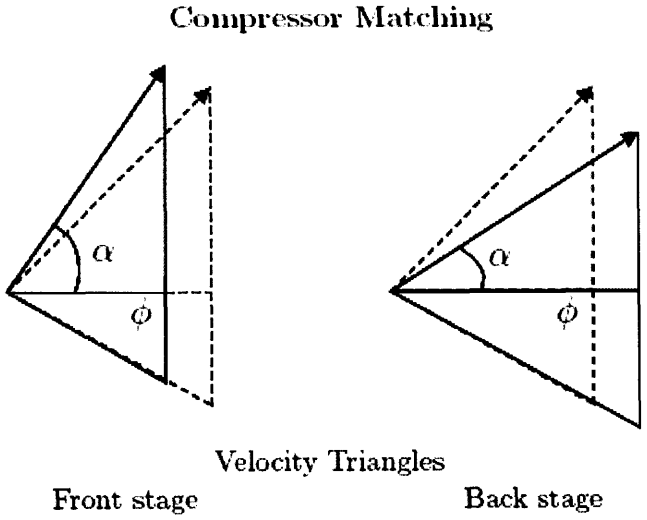


Figure 1.1: Velocity triangles for the front and back-end stages at design condition (dotted line) and at low speed (solid line). (Kerrebrock[9])

increase as shown in Figure 1.1. This change in incidence angles leads the front stages to stall. However, at the back end of the compressor, the pressure is low compared to the design conditions. The flow density is thus also reduced and the flow velocity increases to satisfy mass flow conservation: flow coefficient is high and incidence angles on the blade rows decrease (Figure 1.1). This change leads back end stages to choke. For both the front end and the back end of the compressor, the blade performance and global compressor performance deteriorate.

This simple example shows the difficulty of designing a compressor with high performance at design point and good operability at off-design conditions, i.e., matching the compressor. These problems appeared with the emergence of the design of high-pressure ratio compressors in the 1950s, and compressor designers had to find solutions to alleviate the problem. Figure 1.2 gives two examples: the J57 compressor by Pratt & Whitney designed in 1948 and the J79 compressor by General Electric designed in 1952.

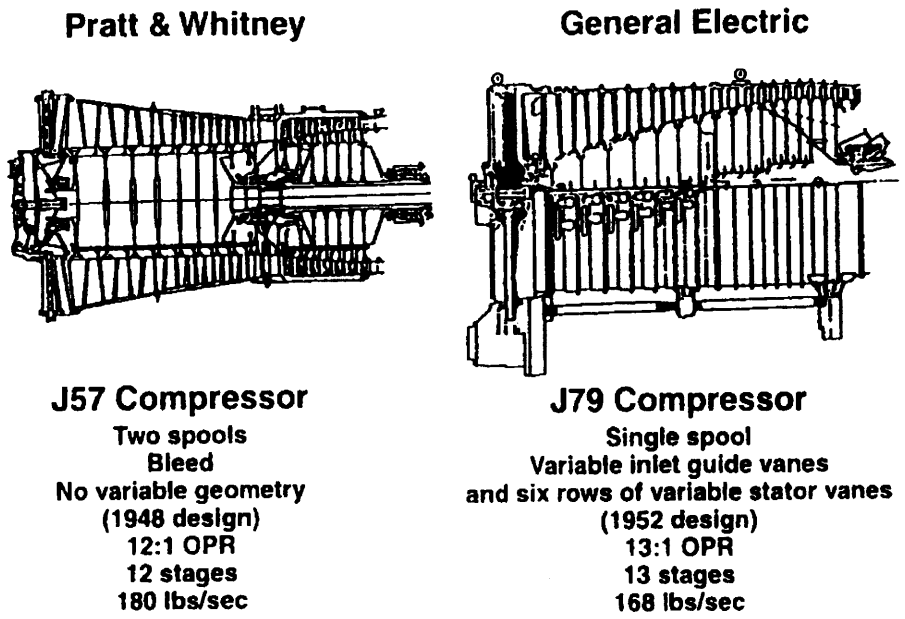


Figure 1.2: Two early high-pressure ratio, multi-stage compressors and their characteristics.

Pratt & Whitney divided the compressor spool into two distinct parts to achieve a higher rotor speed at the back end of the compressor than at the front end. Pratt & Whitney also introduced air bleeds to decrease the mass flow at the rear of the compressor and thus accommodate for the lower density at low speed. GE introduced the solution of variable stator vanes: variable inlet guide vanes and six rows of variable stator vanes were implemented to modify blade angles and accommodate variations in flow angle.

Modern low-pressure compressors usually have fixed geometry, since they have no room for variable-geometry blade rows. Also, variable-geometry blade rows and multiple shafts yield a dramatic increase in engine weight and structural complexity. Thus, a real challenge in striving for high thrust-to-weight ratios is to match multi-stage compressors without using any of the above solutions.

1.1.2 Compressor Stability

Compressors are subject to two types of instabilities, as presented in Figure 1.3. The first, on the left, is called surge and is a large scaled, one-dimensional, low-frequency oscillation of the compressor mass flow. The second, rotating stall, is a rotating flow disturbance produced by the separation of the flow from the compressor blades. Once the flow separates from an airfoil, the incidence angle on the next airfoil increases, causing flow separation on the next airfoil. The flow disturbance propagates around the compressor annulus. While in rotating stall, the compressor operates at roughly steady reduced mass flow and pressure rise.

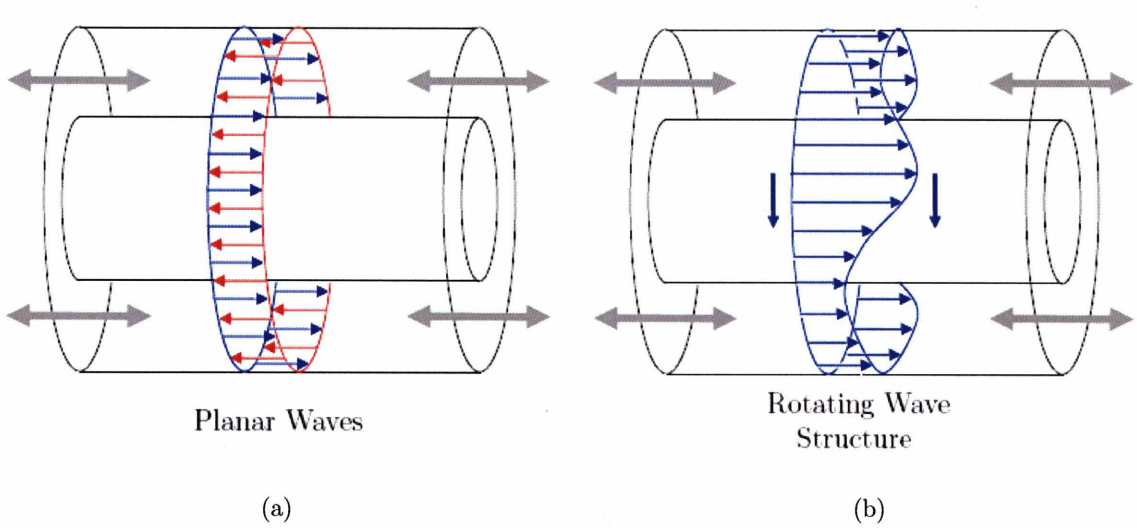


Figure 1.3: Types of compressor instabilities: a. surge: low-frequency average mass flow oscillations and b. rotation stall: local mass flow variations with rotating wave structures

For a given rotor speed these phenomena occur for a low value of mass flow passing through the compressor. They can damage and reduce the life of the engines. Preventing these phenomena from taking place within the compressor increases engine lifetime and reduces the costs of maintenance.

There are two criteria to assess the stability of a compressor. The first is a static stability criterium (Greitzer [8]). The steady-state operating point of the compressor is, as shown in Figure 1.4, at the intersection of the compressor characteristic and the throttle line. Static stability requires that the operating point move back toward its location after a small perturbation in mass flow.

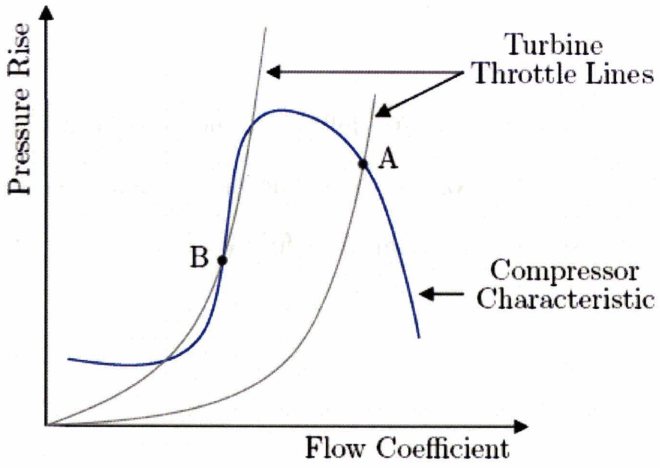


Figure 1.4: Compressor static stability: Point A is statically stable; point B is statically unstable

Figure 1.4 shows that the throttle line must have a slope higher than the compressor characteristic. At location A, if the mass flow decreases, pressure in the combustion chamber becomes higher than needed by the turbine, and more mass flow is pumped through the compressor. At location B, however, the same decrease in mass flow leads to a pressure in the combustion chamber too low for the turbine to maintain the mass flow; therefore the mass flow through the engine decreases. Thus, point A is statically stable, point B is statically unstable.

The surge margin characterizes compressor stability by measuring the margin between

the operating point, and the unstable point or surge point. There are two different ways of measuring the margin or "distance" between the operating point and the surge line. In industry practice, the surge margin refers to the margin between the operating point and the surge point at the same corrected mass flow. Industrial surge margin is defined as:

$$SM_{Ind} = \left. \frac{\pi_{Surge} - \pi_{Operating}}{\pi_{Operating}} \right|_{corrected\ mass\ flow} \tag{1.1}$$

This definition of surge margin is used to account for uncertainties in the corrected speed — during gas turbine acceleration, for example. According to Cumpsty [2], for operation at constant corrected speed, the surge margin definition should take into account the change in compressor outlet flow, a measure of the throttling process which is necessary to take the compressor into stall. The NASA surge margin definition follows this recommendation:

$$SM_{NASA} = 1 - \left. \frac{\pi_{Operating} \cdot \dot{m}_{corr,\ Surge}}{\pi_{Surge} \cdot \dot{m}_{corr,\ Operating}} \right|_{corrected\ rotor\ speed} \tag{1.2}$$

The second criterion for stability refers to dynamic stability and is usually violated first. Greitzer [8] explains that while static instability is associated with a pure divergence from the operating point, dynamic instability is associated with growing oscillatory motions.

Rotating stall and surge phenomena are the mature forms of small amplitude perturbations in the flow field ([13]). Dynamic stability is concerned with the evolution and growth of these small amplitude perturbations. The value of the growth rate of the perturbation determines whether or not the compression system is dynamically stable. If this growth rate is positive, the perturbations grow exponentially and lead to compressor surge or stall. However, if the growth rate of the perturbations is negative, the perturbations are damped and the compressor is stable.

Moore and Greitzer [13] found that the the growth rate of the perturbations σ is proportional to the slope of the non-dimensional total-to-static compressor characteristic:

$$\sigma = \frac{\frac{\partial \Psi_{ts}}{\partial \Phi}}{\frac{2}{|n|} + \mu} \tag{1.3}$$

with

$$\mu = \sum_{blade_rows} \frac{c_x^2}{r \cos^2 \gamma} \tag{1.4}$$

where Ψ_{ts} is the non-dimensional total-to-static pressure rise coefficient, Φ is the flow coefficient, n is the harmonic number, μ is the total blade row (rotor and stator) inertia, c_x is the blade axial chord, r is the blade row mean radius, and γ is the blade stagger angle.

In the compressor model used in the Moore-Greitzer theory, the effects of the blade rows on the compressor stability are all taken into account through a single inertia parameter. The compressor model used throughout this thesis differs in that it captures the effects of each blade row on the flow-field perturbations separately. Independently considering the effects of each blade row on the compressor stability enables one to design each blade row to maximize compressor stability. Hence this compressor model is appropriate for a compressor design problem. This compressor model used in this thesis will be discussed later in Chapter 2.

1.2 Previous Work

1.2.1 Stall Inception and Active Control

Since the early work of Emmons [5] in 1955, stall inception has been studied by numerous researchers. Moore [12] and Moore and Greitzer [13] provided the basis for many investigations, by developing a flow model for axial compressor able to predict compressor stall. The Moore-Greitzer model assumes the existence of circumferential traveling disturbances prior to compression system instability. Experimental work by McDougall et al [11], Garnier et al [7], gave a validation to this assumption. Predicting compressor instability and measuring pre-stall flow perturbations enables the active control of the compression systems to modify their stability and operability. This idea was first articulated by Epstein et al [6]. A summary of the recent research done in the field of active control is provided by Paduano et al [14].

1.2.2 Dynamic Stability Metric

Castiella [1] compared the industrial surge margin and NASA surge margin with the growth rate of the flow-field perturbations for a 3-stage generic compressor to show that neither of the two surge margin definitions correlate with dynamic stability. Based on these observations, Castiella [1] developed a new stability metric using dynamic stability considerations. The new stability metric, denoted by S_d, consists of two parts: 1) the growth rate of the flow-field perturbations, and 2) the robustness of the compression system stability as related to changes in the operating conditions. In concert with the Moore-Greitzer theory, the first part is related to the slope of the total-to-static non-dimensional compressor characteristic. The second part takes into account the shape of the compressor characteristic in

order to guarantee the robustness of the compressor stability as related to changes in the operating conditions.

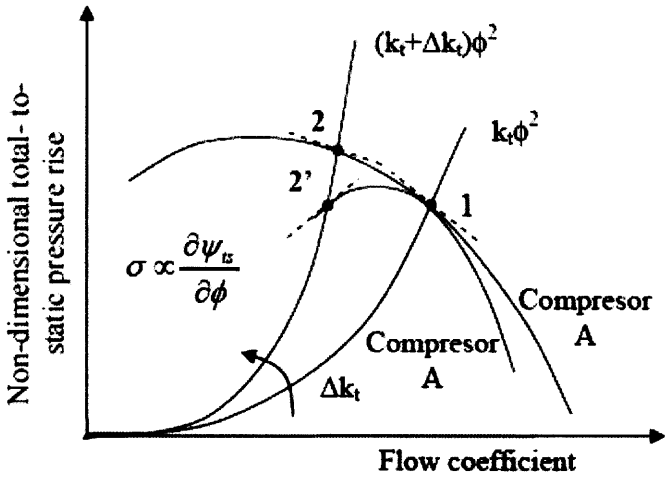


Figure 1.5: Two compressors with the same growth rate of flow-field perturbations at point 1 but with different robustness (adopted from Castiella [1])

As shown in Figure 1.5, compressor A and B have the same growth rate of flow-field perturbations at condition 1, but for the same change in throttle area, compressor A remains stable (the slope of the characteristic is still positive at point 2) and compressor B becomes unstable (the slope of the characteristic is negative at point 2'). This difference between compressors A and B is taken into account in the S_d metric via the robustness parameter R. The S_d metric is defined as follows:

$$S_d = w_\sigma \left(\frac{\sigma}{\sigma_{ref}} \right) + w_R \left(\frac{R_{ref}}{R} \right) \tag{1.5}$$

where σ is the growth rate of the flow-field perturbations and R is defined as the geometric average of the derivative of σ with respect to the location on the characteristic (throttle

coefficient k_t) for M points on the characteristic:

$$R = \left(\prod_{i}^{M} \left. \frac{\partial \sigma}{\partial k_t} \right|_{k_{ti}} \right)^{\frac{1}{M}} \tag{1.6}$$

In the following example, two compressors A and B (Figure 1.6) demonstrate the benefit of the S_d metric as compared to surge margin. Compressors A and B feature the same operating line and surge line. However, their characteristics are vastly different: compressor A has steeper characteristics than compressor B across the full compressor map.

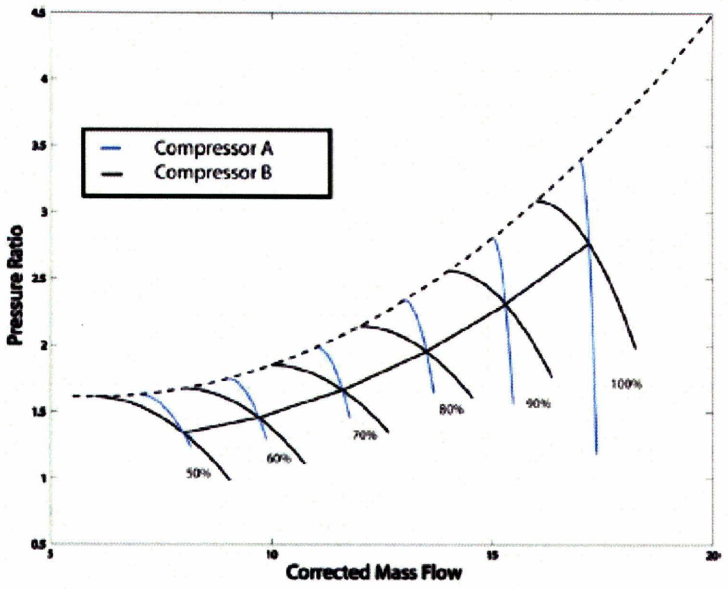


Figure 1.6: Compressor maps of compressors A and B (adopted from Castiella[1])

Examining the evolution of stability metrics with rotor speed shows that, contrary to the surge margin, S_d reveals major differences in the stability of these compressors. As can be seen in Figure 1.7, the industrial surge margin is the same for compressor A and B at every speed and the surge margin defined by NASA reveals a reduction in stability with speed for both compressors. But the S_d metric shows a deterioration in stability for compressor B and

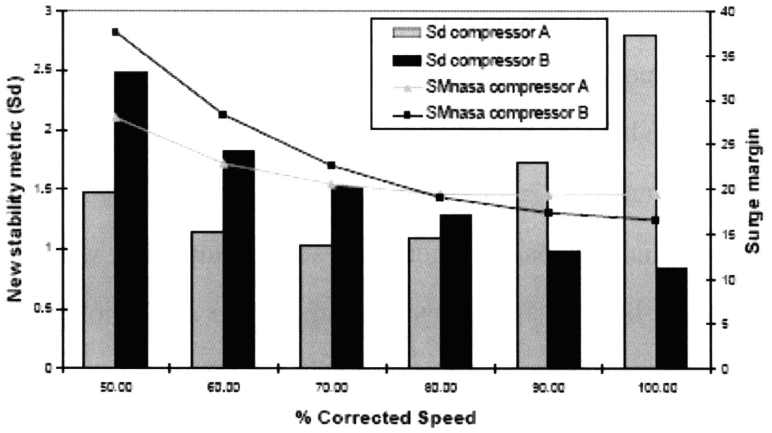


Figure 1.7: S_d versus SM_{NASA} for compressors A and B of figure 1.6 (adopted from Castiella [1])

an increase in stability for compressor A. At low speed, compressor B yields higher levels of robustness than compressor A. However, compressor A's stability increases with rotor speed due to the stabilization of the flow-field perturbations. This example demonstrates that, as opposed to surge margin, S_d is able to capture quantitatively the dynamic stability of the compression system. Finally, this result suggests to use S_d as a compressor design variable to enable compressor designs with enhanced dynamic stability.

1.2.3 Generic 3-Stage Compressor Design Optimization

In order to assess the benefits of using an optimization framework to design compressors with enhanced performance and stability, Castiella [1] applied an optimization framework to a generic 3-stage compressor. Castiella tried two optimization strategies to optimize the performance and stability of the compressor, one using S_d in the objective function, the other using the efficiency. The optimizations produced encouraging results. The dynamic stability of the compressor could be improved by 23% using the S_d-based objective function. The surge

margin SM_{ind} also increased by 3.8 points throughout the operating envelope. The efficiency could be improved by one point on average across the compressor map using the efficiency-based objective function. In both cases, altering the blade geometry to modify the compressor matching achieved improvement. It is important to note that the level of improvement should be regarded with caution since the baseline generic 3-stage compressor was matched far from optimum. The motivation behind this thesis is to apply the methodology to an industry-strength problem and to rigorously assess the feasibility of this idea.

1.3 Nature of the Issue

The compressor studied in this research is a modern 6-stage low-pressure compressor from industry. This compressor yields relatively low stability at flight idle conditions. The goal is to investigate whether flight idle surge margin SM_{ind} can be improved through a better matching of the stages while maintaining the compressor performance at high power. The compressor has no room for variable geometry blade rows; therefore, the question is whether flight idle stability can be improved by optimizing the compressor matching for maximum surge margin at low speed with performance constraints at high speed.

Applying the compressor design optimization framework to this industry strength problem implies that specific tools need to be developed. In particular, a mean-line flow solver must be developed and adapted to this 6-stage compressor in order to estimate with accuracy the compressor performance and compare it to performance measurements provided by industry.

The strategy used to achieve an improvement in flight idle surge margin consists of applying several compressor design optimizations that differ in terms of objective function, stability metric, constraints, and initial condition.

1.4 Scope of the Thesis

The challenge behind this thesis is to improve the flight idle surge margin of an actual low pressure compressor from industry, while maintaining its performance and stability at high power during climb and cruise. Since the low pressure compressor architecture has no room for variable stator vanes, improvements must be achieved by rematching the compressor. The idea is to employ a compressor design optimization framework that combines a blade-to-blade solver with a dynamic compressor-stability analysis to optimize the compressor blade-row geometry. This optimization is done using different strategies, that is, different objective functions and different stability metrics, to search for the best compressor matching solution.

1.4.1 Goals

The success goal defined by the project sponsor is to achieve an improvement in the flight idle (43% speed) surge margin SM_{ind} of three points at a cost of less than a 1% drop in pressure ratio and a one point drop in efficiency at high speed during climb (108% speed) and cruise (100% speed).

Another aim of this thesis is to implement and evaluate the design methodology and framework on an industry-strength problem and to assess potential benefits of a dynamic-stability metric as compared to surge margin considerations.

1.4.2 Research Questions

This thesis addresses the following research questions:

- An accurate estimation of datum-compressor performance is of the utmost importance to the optimization effort since any performance improvement is sensitive to the baseline performance. This raises the question of whether the measured compressor

performance can be adequately estimated using a mean-line compressor performance calculation. Put another way: what level of detail is necessary in the mean-line code and how would one account for three-dimensional loss and endwall effects?

- In previous work by Castiella [1], the optimization methodology applied to a simple generic compressor yielded encouraging results, but is this design optimization methodology applicable to industry-strength design problems?

- What benefits in operability can be achieved if the compressor design is optimized based on the surge margin SM_{ind} or on the dynamic-stability metric S_d?

1.4.3 Technical Roadmap

The design optimization methodology implemented in this research is computer-based, with an objective function based on compressor performance and/or stability metrics. The optimizer searches the space of possible compressor geometries to minimize the objective function. The possible compressor geometries are geometries for which the gas path is unaltered but the stagger and camber angles of the blades rows are changed (except for the fan rotor and the last stator of the machine). The optimizer thus forms the central part of the framework. The optimization framework is shown in Figure 1.8 and consists of three distinct modules: the optimizer, the blade-performance prediction module, and the compressor performance and stability prediction module.

1. The optimizer uses Matlab's optimization toolbox function "fmincon," which implements a sequential, quadratic programming algorithm (SQP) commonly used for constrained non-linear problems. Once the problem variables, the objective or cost function, and the constraints are specified, the optimizer finds a minimum of the objective function. This

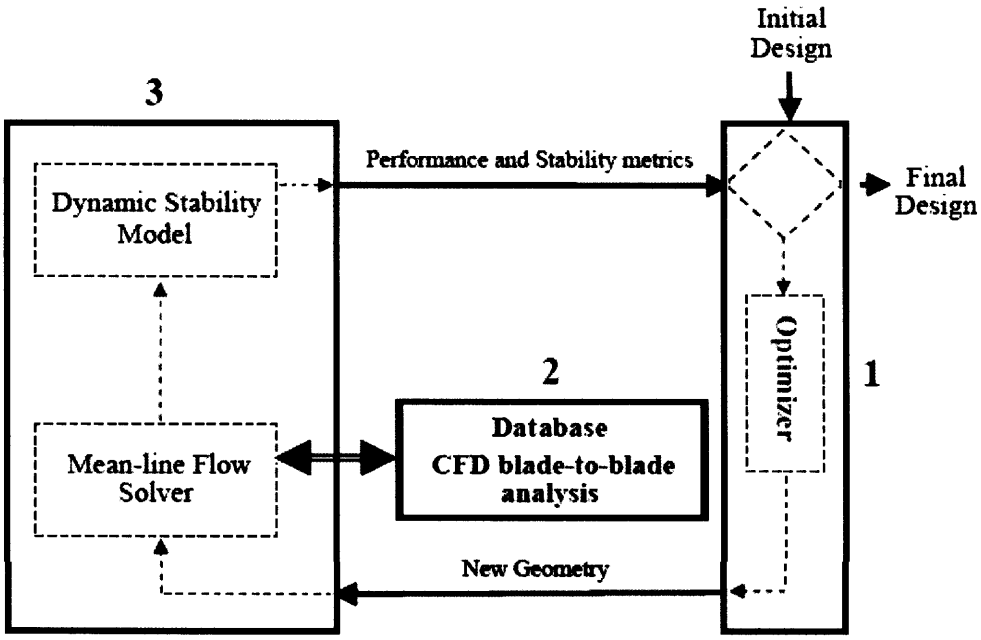


Figure 1.8: Optimization Framework

optimization problem has a total of 20 variables: the stagger and camber angles of stator 1 to rotor 6 blade rows. The objective function to be minimized is a combination of compressor performance and/or stability metrics evaluated at different operating conditions. And finally, the problem constraints require that the high-speed pressure ratio drop at operating point (100% and 108% speed) does not exceed 1% of the baseline value, and that the high-speed efficiency drop at operating point (100% and 108% speed) does not exceed one point. Compressor geometries for which high-speed pressure ratio and efficiency requirements are not satisfied are not taken into account by the optimizer.

At every iteration, the optimizer defines a new compressor geometry for which the objective function must be evaluated. Evaluating the objective function is the purpose of the two other modules of the framework: the compressor performance and stability prediction module (module 3) and the blade-performance prediction module (module 2).

2. The role of the blade-performance prediction module is to provide blade-row performance parameters such as deviation angle, profile loss, and profile-loss derivative with

respect to flow angle. These parameters are specific to the new blade geometries defined by the optimizer and to the flow conditions — Mach number and flow angle — specified by the compressor performance and stability module.

Running in real time both an optimization and a CFD software to compute blade-row performance for each new blade profile would require months of calculation. To reduce the computing time required by the optimizer, a database is established that contains blade row performance information for a very large number of possible blade profile geometries. The database can be created before carrying out the optimization effort, so the computing time can be minimized.

3. The compressor performance and stability prediction module evaluates the objective function for a new compressor geometry defined by the optimizer. This module uses required blade row performance data provided by module 2 in the framework. This part combines a mean line flow solver and the dynamic stability compressor model developed by Spakovszky [16].

The mean line flow solver uses the blade angles from module 1 and the blade profile loss and deviation angles from module 2 to compute compressor pressure ratio and efficiency. The dynamic stability compressor model uses the blade geometries and the associated profile-loss derivatives with respect to flow angle from module 2 to predict compressor stability. Combining these two tools allows one to construct the part of the compressor map needed to evaluate the objective function. Module 3 finally sends back to the optimizer the value of the objective function and the pressure ratio and efficiency at high speed to check if the constraints are satisfied.

In summary, at every iteration, the optimizer (module 1) generates a new compressor and then module 2 and 3 compute the new compressor map and evaluate the objective function. Finally, the result is returned to the optimizer which repeats the process depending on the value of the objective function.

1.4.4 Outline of the Thesis

The thesis is organized as follows. Chapter 2 provides a description of the optimization framework's module 3 , including the mean-line flow analysis and the dynamic stability compressor model. Chapter 3 explains how the blade performance database is defined and computed. The datum compressor performance and stability estimation are then discussed in Chapter 4. Chapter 5 presents the implementation of the optimization framework to the compressor matching problem at hand. The results of the compressor design optimization strategy applied to the datum compressor are presented in Chapter 6. Finally, Chapter 7 summarizes the approach of the project and the results, and gives some recommendations for future work.

Chapter 2

Datum Compressor Performance and Stability Estimation

This chapter describes how the datum-compressor performance and stability are estimated using a mean-line flow calculation code and a previously developed dynamic-stability compressor model. The methodology used to estimate the datum-compressor performance and stability is also used as module 2 of the optimization framework to predict the performance and stability of each new compressor defined by the optimizer.

For each set of operating conditions (mass flow and rotor speed), the mean-line flow calculation calculates the compressor pressure ratio and the compressor efficiency. The *dynamic-st*ability compressor model predicts if the compressor is stable or not. Combining these two tools enables one to determine the complete compressor map, including the surge line.

2.1 Compressor Performance Estimation

2.1.1 Overview

The 6-stage low-pressure compressor under investigation can be divided into the fan-root section followed by a $5\frac{1}{2}$-stage LPC. The gas path is shown in Figure 2.1 and Figure 2.2 shows the LPC blade rows. The idea of the research is to optimize the LPC matching by modifying the blade row geometry of stator 1 through rotor 6. The fan root cannot be altered, and a specific model is developed to estimate its performance.

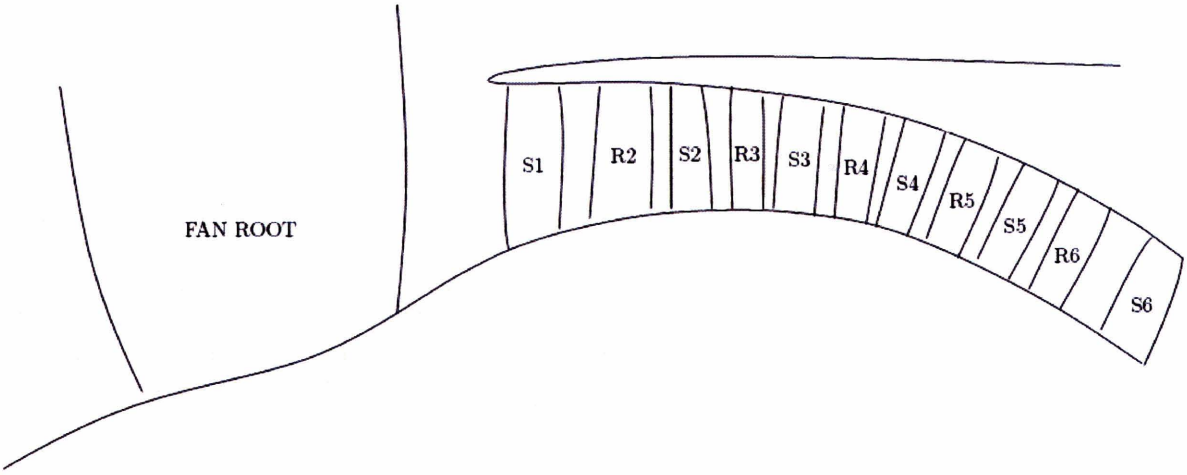


Figure 2.1: Sketch of the gas-path geometry of the 6-stage low-pressure compressor investigated

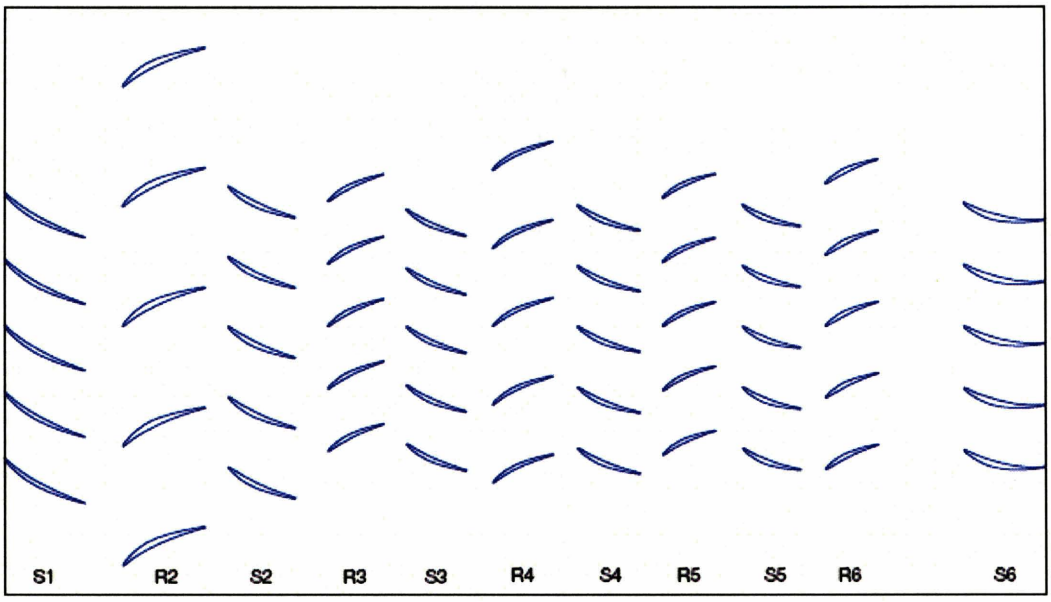


Figure 2.2: Low pressure compressor blade rows

The LPC performance is estimated using a mean-line flow calculation that involves to two successive steps: 1) estimating the operating line and, 2) estimating off-design performance.

2.1.2 Fan Root Model Description

The main difficulty in describing the fan-root performance arises from the fact that the separation between the flow entering the core of the engine through the low-pressure compressor and the bypass flow happens downstream of the fan. The flow-path area across the fan root is thus undefined and varies with the rotor speed and the mass flow.

Since the fan root is not included in the optimization, a simple fan-root model is established and used to estimate the compressor performance. The model assumes that the fan-root loss and loading depend on rotor speed only and are thus held constant for a given speed. Consequently, the flow path area upstream and downstream of the fan root depends *only* on rotor speed. The main parameters defining the fan-root model are:

- Flow-path area upstream and downstream of the fan root
- Fan-root loss
- Fan-root loading
- Fan-root loss coefficient derivative with respect to flow angle ($\frac{\partial \omega}{\partial \beta}$) necessary for the dynamic stability compressor model

Measurements of the flow-path areas upstream and downstream of the fan and of the fan loss and loading at 40%, 60%, 80%, and 100% speed operating point were supplied by

industry. The fan-root $\frac{\partial \omega}{\partial \beta}$ parameter is adjusted to match the surge point on these four speed lines to the data. A linear interpolation with rotor speed provides the value of these four parameters at any rotor speed.

At low speed (below 60% speed), the fan performance depends on the mass flow. Since the model needs to account for this, a mass flow dependance is added to the fan parameters. Finally, at under 60% speed, the parameters of the fan root model depend on rotor speed and mass flow.

2.1.3 Compressor Performance Estimation at Design Conditions

The purpose of this step is to estimate accurately compressor pressure ratio and efficiency at each operating point. To ensure that the compressor is correctly matched, velocity triangles at the mean streamline are compared with the industry-supplied data. To estimate the global compressor performance, a model accounting for endwall effects is added to the mean-line calculation.

The first step in the compressor performance estimation at operating conditions is thus to determine the velocity triangles. Industry-supplied data provides velocity triangles at each axial location of the compressor, blade-row loss, and flow states for every streamline. This data was generated using a streamline code and experimental data. First, industry blade loss and deviation corresponding to the mean streamline is used in the mean-line flow calculation. The velocity triangles thus calculated are compared to the velocity triangles from the data. Then blockage at each axial location of the compressor can be determined by matching the calculated meridional flow velocity with the meridional flow velocity supplied

by industry. The blockage is defined as:

$$k = \frac{A_{actual}}{A_{effective}} \quad . \tag{2.1}$$

Industry data is provided only for 40%, 60%, 80% and 100% speed operating points. Therefore, blockage is determined only for these operating points. Linear interpolation is used to determine the blockage at other rotor speeds. The blockage is assumed independent of mass flow.

The next step involves using computed blade deviation angles in the mean line flow calculation. The deviation angles are estimated using: 1)the deviation angle provided by MISES that varies with rotor speed and mass flow, 2) a correction δ_{row} specific to each blade row linearly dependant on rotor speed only.

For the same blade profile, deviation angles computed using the blade-to-blade flow solver MISES slightly differ from the deviation angles found in industry data. Therefore, a small correction δ_{row} is added to the deviation angle given by MISES. These corrections δ_{row} depend only on the rotor speed.

The last step consists of accounting for endwall losses in the mean-line calculation. The blade row stagnation pressure loss is determined using: 1) the blade profile loss (2D) computed in MISES which varies with rotor speed and mass flow and, 2) a "3D/2D" loss coefficient specific to each blade row, a linear function of the rotor speed only, to account for endwall losses. The 2D loss is multiplied by a "3D/2D" loss coefficient. For each blade row, the "3D/2D" loss coefficient is determined based on the ratio of the mass-average loss over the loss at the industry-provided mean streamline. Figure 2.3 shows a schematic description of the "3D/2D" loss coefficients.

Since industry data is provided for 40%, 60%, 80%, and 100% speed only, the "3D/2D"

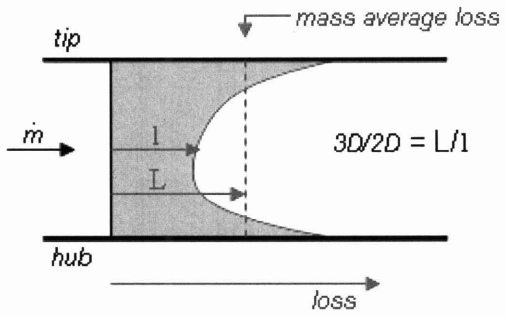


Figure 2.3: "3D/2D" loss coefficient description

loss coefficients are first determined for these speeds. Linear interpolation is used to calculate the "3D/2D" loss coefficients at any rotor speed. This 3D loss model is deemed sufficient for this application and as will be shown later, this model adequately estimates of compressor performance.

2.1.4 Off-Design Performance Estimation

The shape of the speed lines at off-design conditions depends mainly on the blade-row loss and deviation angles that vary with mass flow. In order to account for the streamline contraction and endwall effects, the LPC is divided into three compressor blocks, as shown in Figure 2.4. This enables altering the loss and loading of a given part of the compressor independently. For a given rotor speed, a loss multiplier and a deviation-angle multiplier is applied to each compressor block. They enable light modifications of the loss and loading of the corresponding block and modify the shape of the speed line.

As shown in Figure 2.5, the estimated speed line (the pressure ratio and efficiency curves) is compared to the industry data. Loss and deviation multipliers can be chosen to match

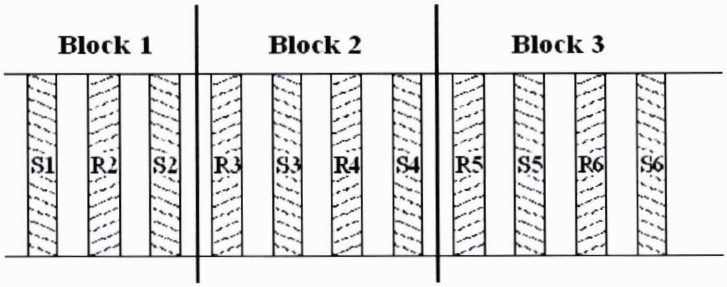


Figure 2.4: The low-pressure compressor is divided into three distinct compressor blocks

the two curves. This process is done iteratively to obtain an adequate level of accuracy.

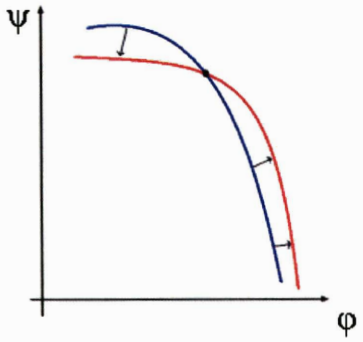


Figure 2.5: Speed line adjustment: The blue speed line is modified to match the industry data in red (this is a sketch and is not to scale).

Loss and deviation multipliers are determined for 40%, 60%, 80%, and 100% speeds. In between these speeds, loss and deviation multipliers are linearly interpolated.

The compressor map can be constructed using the fan root and the simple endwall loss models. The assumption is made that these models do not change with the compressor design. Therefore, the parameters introduced (correction to deviation angles, "3D/2D" loss coefficients, and loss and deviation multipliers) are kept the same during the optimization effort.

During the optimization, the optimizer defines a new compressor geometry at every

iteration. To evaluate the objective function, the compressor map of the new compressor is predicted using the same performance estimation methodology as for the datum compressor.

2.2 Compressor Stability Estimation

2.2.1 Dynamic Stability Compressor Model

The compressor model used throughout this thesis is a model developed by Spakovszky [16]. As mentioned in the first Chapter, this compressor model differs from the model used by Moore and Greitzer in that it captures the effects of each blade row on the flow field perturbations separately. The dynamic-stability compressor model makes the following assumptions:

- Flow is incompressible[1](Mach number assumed small enough)
- Reynolds number effects are neglected
- Small perturbations are assumed so that the problem can be linearized
- Hub-to-tip ratio is high enough to assume two-dimensional flow
- Viscosity and heat transfer are neglected in the inlet and exit ducts and in the inter-blade-row gaps.
- Blade row unsteady deviation effects are neglected
- The blade rows are modeled as semi-actuator disks with unsteady blade-passage fluid inertia and unsteady loss terms.

[1]Note that all mean flow quantities used in this model are based on the compressible mean-line performance estimation and that the incompressible flow assumption is only made for small perturbations of the flow field (i.e. entropy waves are neglected).

A dynamic analysis is performed for each of the compression system's component: rotor and stator blade rows, and also inlet, exit and inter blade-row axial gaps. These compressor components are shown in Figure 2.6.

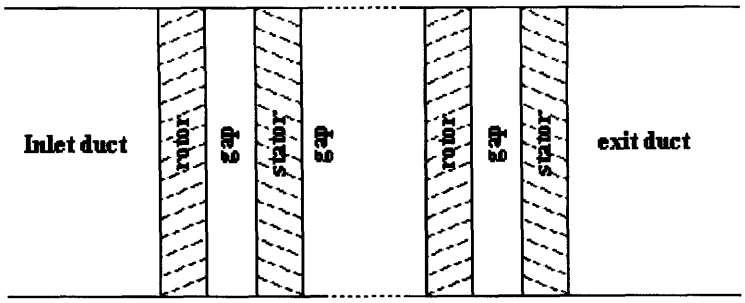


Figure 2.6: Representation of the compressor in the dynamic stability model

For each component, the governing equations are linearized and solved for the perturbation in pressure, meridional, and angular velocity. The flow perturbations are broken down into perturbation harmonics using Fourier series. For each harmonic, the system of equations relating the downstream perturbation to the upstream perturbation can be written in a matrix form to give the component's *transmission matrix.* (For a detailed derivation, see Spakovszky [16]). The transmission matrices yield three fundamental types of perturbations: two potential-like perturbation types or potential modes (denoted A_n and B_n for n-th harmonic) and one vortical perturbation type or vortical mode (C_n).

For an axial gap, the transmission matrix for the n-th ($n > 0$) harmonic is:

$$T_{ax,n} = \begin{bmatrix} e^{nx} & e^{-nx} & e^{-(\frac{-s}{\overline{V}_x}+jn\frac{\overline{V}_\theta}{\overline{V}_x})x} \\ je^{nx} & je^{-nx} & -(\frac{sj}{n\overline{V}_x}+jn\frac{\overline{V}_\theta}{\overline{V}_x})e^{-(\frac{-s}{\overline{V}_x}+jn\frac{\overline{V}_\theta}{\overline{V}_x})x} \\ -(\frac{s}{n}+\overline{V}_x+j\overline{V}_\theta)e^{nx} & (\frac{s}{n}-\overline{V}_x+j\overline{V}_\theta)e^{-nx} & 0 \end{bmatrix} \cdot e^{jn\theta} \tag{2.2}$$

Blade-row transmission matrices depend on the blade geometry and the mean-line flow conditions. Transmission matrices for a rotor-blade row and a stator-blade row can be written as follow:

$$B_{rot,n} = \begin{bmatrix} \frac{1}{AR} & 0 & 0 \\ \frac{\tan\beta_2}{AR} & 0 & 0 \\ \begin{pmatrix} \begin{pmatrix} \tan\beta_2 - \lambda_{rot}(s+jn) \\ -\overline{V}_{x2} - \overline{V}_{\theta 2}\tan\beta_2 \end{pmatrix} /AR \\ -\frac{R_1}{R_2}\tan\alpha_1 - \frac{\partial L_R^{ss}}{\partial V_{x1}}\frac{1}{1+\tau_R(s+jn)} + \overline{V}_{x1} \end{pmatrix} & \overline{V}_{\theta 1} - \frac{\partial L_R^{ss}}{\partial V_{\theta 1}}\frac{1}{1+\tau_R(s+jn)} & 1 \end{bmatrix} \cdot e^{jn\theta} \tag{2.3}$$

$$B_{sta,n} = \begin{bmatrix} \frac{1}{AR} & 0 & 0 \\ \frac{\tan\alpha_2}{AR} & 0 & 0 \\ \begin{pmatrix} \left(-\lambda_{sta}s + \overline{V}_{x2} - \overline{V}_{\theta 2}\tan\beta_2\right)/AR \\ -\frac{\partial L_S^{ss}}{\partial V_{x1}}\frac{1}{1+\tau_S s} + \overline{V}_{x1} \end{pmatrix} & \overline{V}_{\theta 1} - \frac{\partial L_S^{ss}}{\partial V_{\theta 1}}\frac{1}{1+\tau_S s} & 1 \end{bmatrix} \cdot e^{jn\theta} \tag{2.4}$$

For an entire system of compressor components, a system transmission matrix can be obtained by successively multiplying the component transmission matrices. The entire com-

pressor transmission matrix can be computed as follow:

$$T_{sys,n} = (T_{exit,n})^{-1} \prod_{k=Nstages}^{2} (B_{sta,k,n} \cdot B_{middlegap,k,n} \cdot B_{rot,k,n} \cdot B_{upstreamgap,k,n}) \tag{2.5}$$

with

$$B_{upstreamgap,1,n} = T_{inlet,n} \tag{2.6}$$

Specifying inlet and exit boundary conditions finally leads to an eigenvalue problem formulation. The boundary conditions specify that, assuming infinite length ducts upstream and downstream of the compressor, the potential modes can only decay away from the compressor. Upstream flow is also assumed irrotational. The system boundary condition can be written as:

$$\begin{bmatrix} 0 \\ 0 \\ 0 \end{bmatrix} = \begin{bmatrix} EC \cdot T_{sys,n}(s) \\ IC \end{bmatrix} \cdot \begin{bmatrix} A_n(s) \\ B_n(s) \\ C_n(s) \end{bmatrix}_{up}, \quad for\ n > 0 \tag{2.7}$$

$$where \qquad EC = \begin{bmatrix} 1 & 0 & 0 \end{bmatrix} \quad and \quad IC = \begin{bmatrix} 0 & 1 & 0 \\ 0 & 0 & 1 \end{bmatrix} \tag{2.8}$$

Equation 2.7 has a non-trivial solution if, and only if,:

$$det \begin{bmatrix} EC \cdot T_{sys,n}(s) \\ IC \end{bmatrix} = 0 \tag{2.9}$$

For a specified harmonic number, Equation 2.9 returns eigenvalues for all the perturbation

modes. One eigenvalue is written as:

$$s_n = \sigma_n - j\omega_n \tag{2.10}$$

where σ_n and ω_n are the growth and rotation rates of the perturbation wave.

A positive growth rate means that the perturbation is growing exponentially with time and the compressor is unstable. If, on the other hand, the growth rate of the perturbation is negative, the perturbation amplitude decreases with time. If the growth rates of all modes is negative for all the perturbation harmonics, the compressor is dynamically stable. As shown by Castiella [1], the first harmonic of the least stable mode is generally the first one to become unstable. Considering the growth rate of this harmonic only suffices to assess compressor dynamic stability.

2.2.2 Stall Line Estimation

For a given rotor speed, the stall point is defined by the growth rate of the flow-field perturbations σ of zero. Hence, the stall point can be found by computing the compression system eigenvalues. For a first value of mass flow, the dynamic stability analysis provides the eigenvalues of the compression system. If the least stable eigenvalue is negative (if the compressor is stable), the mass flow is reduced; if the compressor is unstable, the mass flow is increased. The new mass flow defines a new point on the speed line and the process is repeated until it finds the neutral stability point of the speed line, at which point the real part of the least stable eigenvalue is zero.

Figure 2.7 shows the eigenvalues of the least stable mode for harmonics 1, 2, and 3 as the mass flow converges towards the mass flow of the surge point. The first harmonic is the first

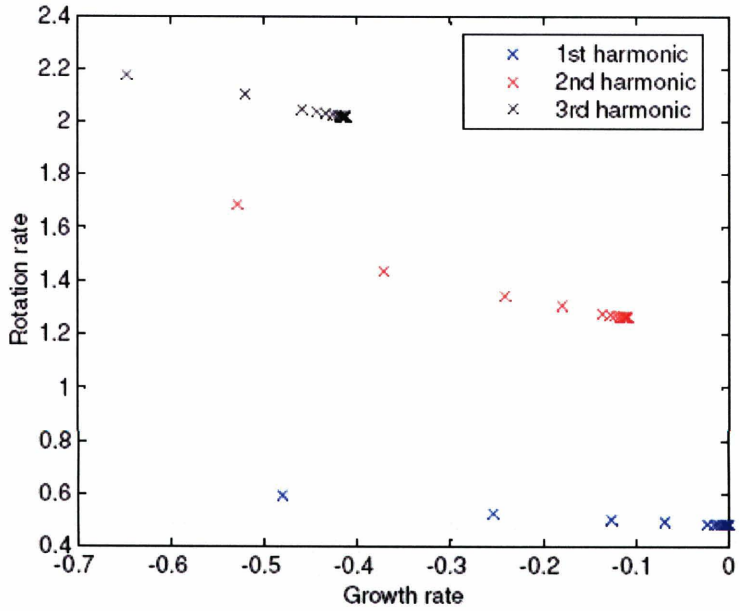


Figure 2.7: Eigenvalues of the harmonics 1, 2, and 3 for operating points at mass flow larger than the mass flow at surge point at design speed.

one to become unstable, and the neutral stability point is reached when the growth rate of this harmonic is zero.

To determine the stall line on the compressor map, stall points at several speeds (for example 40%, 47%, 59%, 71%, 79%, 91%, and 99% speed) are computed using the dynamic-stability model. Then interpolation is used to estimate the stall line on the compressor map.

Chapter 3

CFD Based Blade Performance Database

3.1 Nature of the Issue

To evaluate the objective function for a given geometry defined by the optimizer, numerous points on the compressor map must be calculated. As seen in Chapter two, the calculation for a single operating point on the compressor map requires the computation of deviation angles and profile losses for all of the blade rows. The derivatives of profile loss with respect to axial and tangential velocities are needed as input to the dynamic-stability model. Depending on rotor speed and mass flow, the flow angle and inlet Mach number of each blade row vary. Therefore, to compute the entire compressor map, blade deviation angles and losses are needed for a large range of flow angles and Mach numbers.

Running MISES online with the optimizer for each blade profile defined during the optimization process is too costly in computing time. Hence another approach needs to be found.

One possible approach is to create a database that gathers the required information. This database is created as follows:

- Develop a parametric description of the blade profiles.
- Choose the optimization variables (for example stagger and camber angles) and their

range of possible variation around the datum value. Then discretize the corresponding domain of the possible blade geometries. For every point of this discrete domain, the blade profile is generated using the parametric description of blade profiles and MISES is run to determine blade performance.

During the optimization effort, blade performance for a specific blade geometry defined by the optimizer is calculated using a linear interpolation between the blade performance of the closest blade geometries present in the database.

3.2 Parametric Description of Blade Profiles

One description method needs to capture all of blade profiles defined by the optimizer during an optimization effort, especially the blade profiles of the datum compressor. Blade performance is sensitive to the leading edge of the blade profile and hence, the leading edge must be carefully described. The blade profile is constructed using a camber line to which a thickness distribution is added. Camber line and thickness distribution are parameterized using blade-geometry parameters such as blade angles, chord, and thickness, for example.

3.2.1 Blade-Profile Parametrization

Seven independent parameters are chosen to parameterize the blade camber line and thickness distribution. These parameters are presented schematically in Figure 3.1:

- Axial chord
- Stagger angle (γ)

- Camber angle (θ)
- Ratio unstaggered inlet metal angle κ_1 over camber angle (p parameter $p = \kappa_1/\theta$)[2]
- Blade maximum thickness in percentage of axial chord (t_m)
- Location of maximum thickness in percentage of axial chord (x_m)
- Solidity (σ)

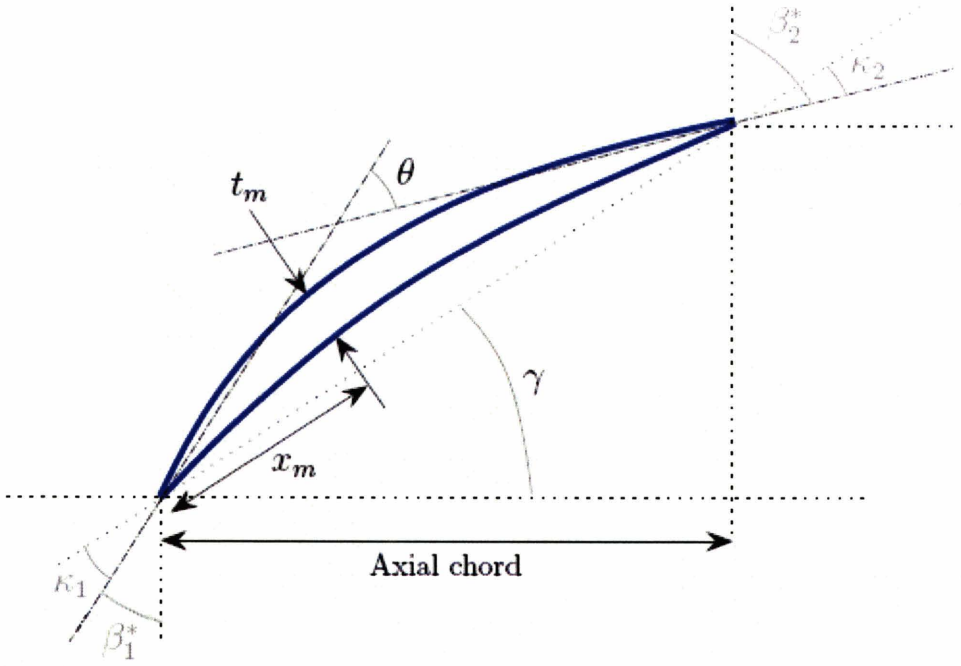


Figure 3.1: Blade profile parametrization

Figure 3.2 defines the flow angles and blade metal angles used in this thesis.

First the camber line is defined in terms of a third-order polynomial that uses information such as stagger angle and camber angle, axial chord, and p parameter. The axial chord and

[2]this parameter is necessary to determine the unstaggered inlet and exit blade angles from the camber angle

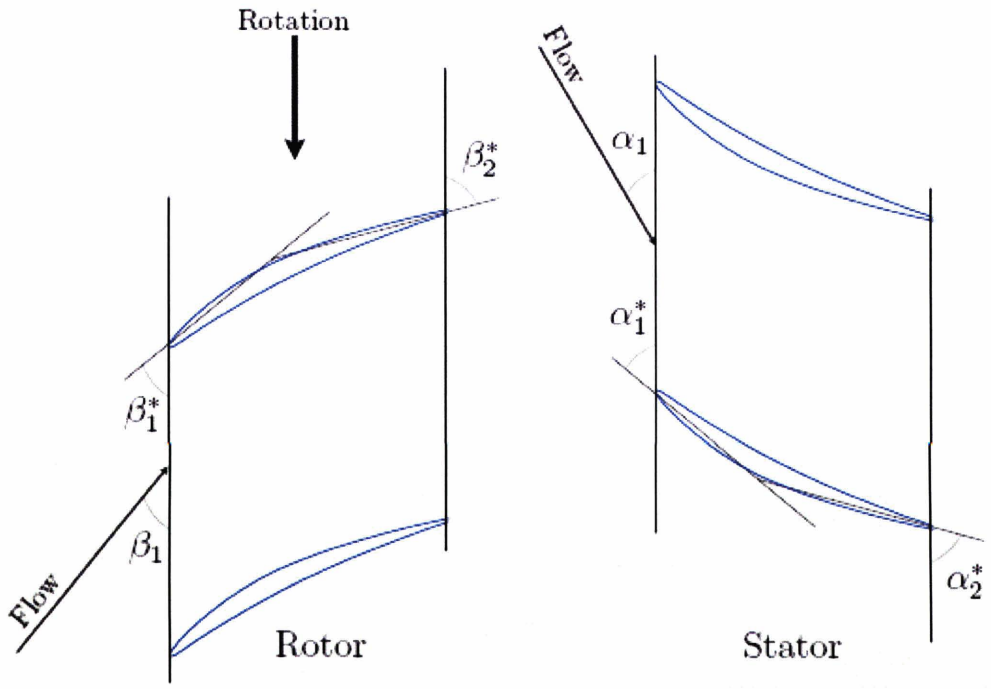


Figure 3.2: Definition of the blade metal angles and flow angles used.

the stagger angle define the camber line endpoint location. The staggered blade-metal angles β_1^* and β_2^* define the camber line slope at the two endpoints as follows:

$$\beta_1^* = \tfrac{\pi}{2} - \gamma - \kappa_1 = \tfrac{\pi}{2} - \gamma - p\theta \qquad \text{and} \qquad \beta_2^* = \tfrac{\pi}{2} - \gamma + \kappa_2 = \tfrac{\pi}{2} - \gamma + (1-p)\theta$$

where κ_1 and κ_2 are the unstaggered blade-metal angles.

3.2.2 Thickness Distribution

A thickness distribution is added to the camber line. The thickness distribution is defined by four Bezier splines that depend on the maximum blade thickness t_m and the location of maximum blade thickness in percentage of chord x_m. The four Bezier splines are shown in Figure 3.3.

Different thickness distributions were tried to match original compressor-blade profiles, and Bezier splines provided the best result. Bezier splines are third-order polynomials defined by four parameters: two endpoints and the slope of the spline at each endpoint.

For each segment of the blade profile, t_m, x_m, and the camber line define the location of the two endpoints of the segment, and the two other parameters can be adjusted to fit the datum-blade profile. Eight parameters thus define the thickness distribution.

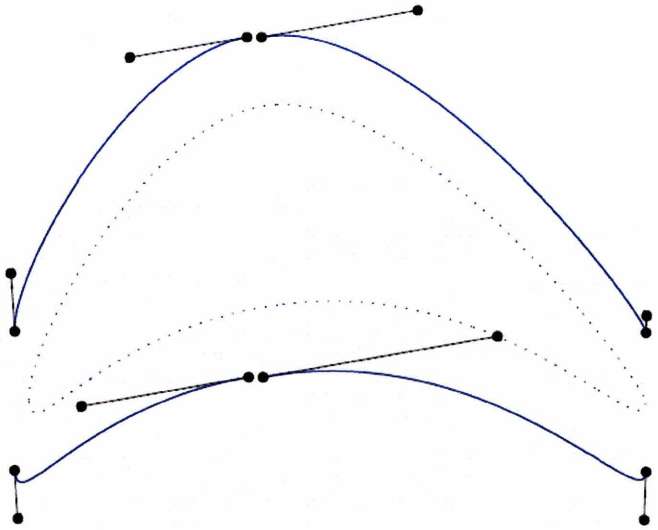


Figure 3.3: Blade-profile parametrization: thickness distribution composed by four Bezier segments. (Figure not to scale)

As shown in Figure 3.4, the parameterized-blade profile compares well with the datum-blade profile. Note that the leading edge is well described.

Each datum-blade profile is parameterized using a unique set of parameter values. During the optimization effort, the optimizer can modify the stagger and camber angles of the blade rows, and all other parameters of the blade description are fixed to their datum values.

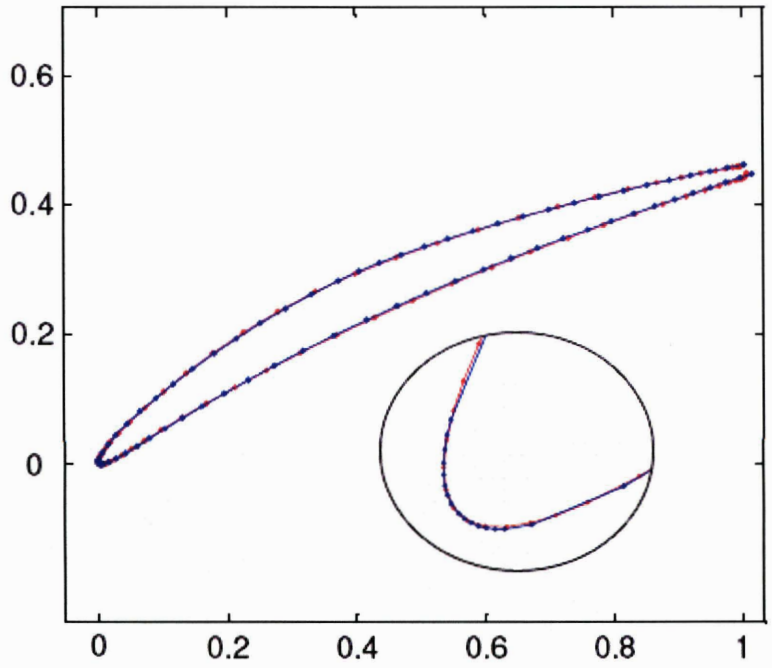


Figure 3.4: Blade-profile parametrization: comparison between datum-blade profile (in red) and parameterized-blade profile (in blue). The two contours are superimposed.

3.2.3 Assessment of Blade Profile Parametrization

Before the database is established, one must make sure that the blade-profile parametric description accurately represents the datum-blade profiles. To assess this, for each blade row MISES computations are conducted and the loss bucket of the parameterized-blade profile is compared to the loss bucket of to the datum-blade profile. Parameter values of the profile description are adjusted until the comparison between loss buckets yields errors less than 1% (Figure 3.5).

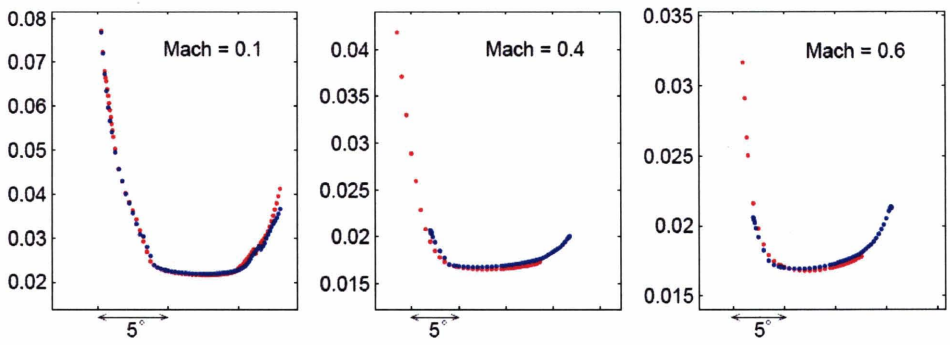


Figure 3.5: Comparison between computed (MISES) loss buckets of the parameterized-blade profile (in blue) and loss buckets of the datum-blade profile (in red). The two loss buckets compare well, and the blade parametrization is assessed. Loss is expressed in terms of loss coefficient versus flow angle.

3.3 Database

3.3.1 Optimization Parameter Choice

The blade parameters that are changed in the optimization effort are the stagger angle and the camber angle. Stagger and camber angles govern the turning of the flow and thus have a major effect on the blade loading, loss, and deviation angle.

One could choose to let the optimizer alter more blade parameters during the optimization effort. However, doing so would increase the computing time required to compute the blade-performance database and run the optimization.

3.3.2 Optimization Parameter Range

To limit the time required to compute a blade-row performance database, the number of values of stagger angle and camber angle in the database is limited to five. So a database for a single blade row consists of 25 data sets. For the stagger and camber angles, the possible values in the database are:

$$[b\text{-}2\delta,\ b\text{-}\delta,\ b,\ b\text{+}\delta,\ b\text{+}2\delta]$$

where b is the datum-angle value and δ is the blade-angle increment value.

For each blade row, δ must be chosen taking into account the loss bucket's sensitivity to changes in blade angle. A large value of δ increases the blade-angle range but decreases the database accuracy. However, a reduced value of δ increases the database accuracy but limits the blade-angle range.

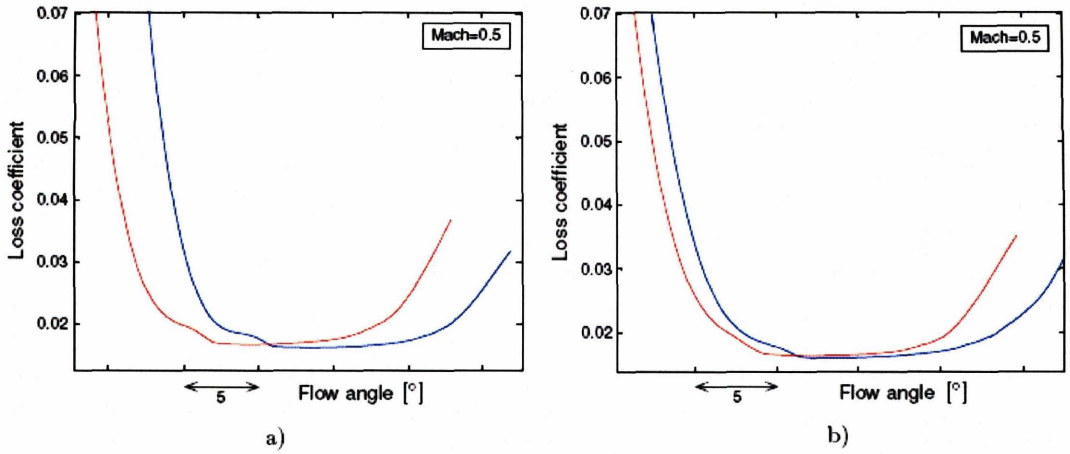


Figure 3.6: Effects of a 4° variation in stagger angle (a) and camber angle (b) on loss buckets. On both plots, the blue bucket corresponds to the lower value of blade angle, and the red bucket corresponds to the higher value of blade angle.

Figure 3.6 shows the loss-bucket sensitivity to camber and stagger angles for Stator 3. On the left, the two loss buckets correspond to blade profiles with the same camber angle and a 4° difference in stagger angle. On the right, the stagger angle is the same for the two buckets, but there is a 4° difference in camber angle. The loss buckets are significantly different, and a 4° range seems large enough for stagger and camber angles. So the δ value chosen for Stator 3 is 1°. As will be seen later, the value of δ ensures adequate database accuracy.

For the back-end stages of the LPC (Stator 3 to Rotor 6), a δ of 1° is chosen. For the front-end stages (Rotor 2 to Rotor 3), δ is equal to 0.5°. Finally, the Stator 1 database requires an enhanced accuracy and a δ of 0.1° while the number of points in the database is increased to 100.

3.3.3 Database Generation

One database is computed for every single blade row from Stator 1 to Rotor 6. In the database, the stagger and camber angles vary, and the other blade-geometry parameters are kept constant at their datum values. Since the datum values of the blade-geometry parameters are different for each blade row (the solidity or the blade chord, for example), a specific database for each blade row is needed.

The computation of the blade performance for all the blade geometries of every database is performed using the blade-to-blade flow solver MISES. For each blade geometry, MISES provides the blade performance for inlet Mach numbers from 0.1 to 0.78. For each of these Mach numbers, the blade performance is calculated for a large range of flow angle using a 0.5° flow-angle increment.

Chapter 4

Datum Compressor Performance

4.1 Implementation of Compressor Performance Estimation Method

Following the methodology described in Section 2.1, the blockage along the LPC, the corrections to blade-deviation angles, and the "3D/2D" loss coefficients are computed for the datum compressor. Figures 4.1, 4.2, and 4.3 show these parameters for 40%, 60%, 80% and 100% speed. Blockage is defined as follows and yields values greater than 1.

$$k = \frac{A_{actual}}{A_{effective}} \tag{4.1}$$

The unsteady loss time lag of the blade rows uses a proportionality constant τ_u which is set to the common value of 1.5. τ_u is defined as:

$$\tau_{R/S} = \tau_u \frac{c_x}{r \cos\gamma \bar{V}_x} \tag{4.2}$$

where τ_R and τ_S are the rotor and stator unsteady loss time lag. r is the radius and $\bar{V}_x$ is the mean meridional flow velocity and c_x and γ are the blade axial chord and stagger angle.

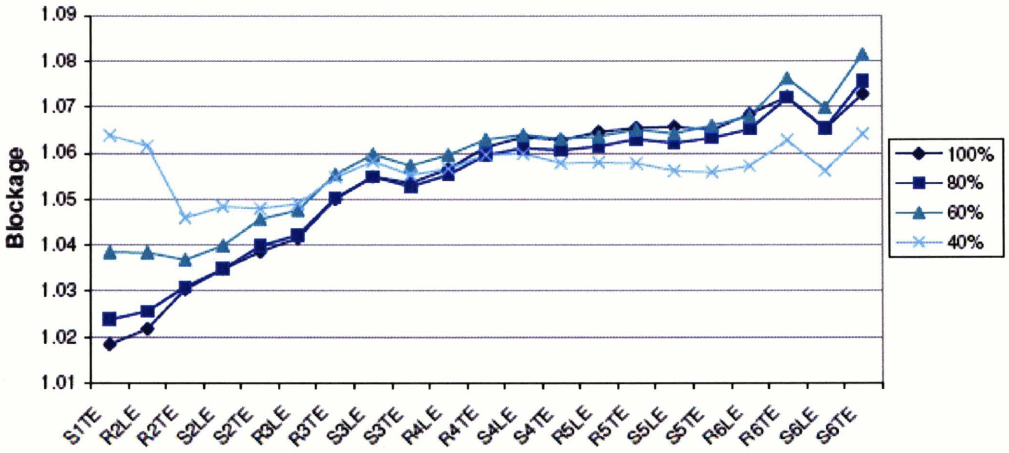


Figure 4.1: Blockage at each compressor axial location from Stator 1 trailing edge to Stator 6 trailing edge.

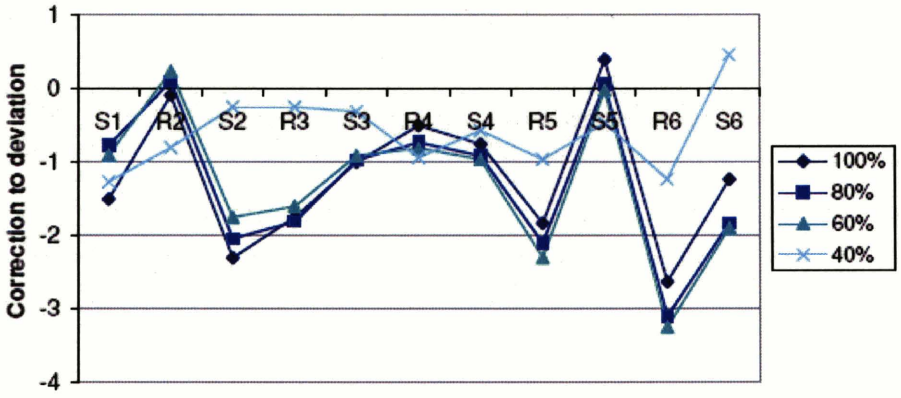


Figure 4.2: Corrections (in degrees) added to the blade-row deviation angles for different rotor speeds.

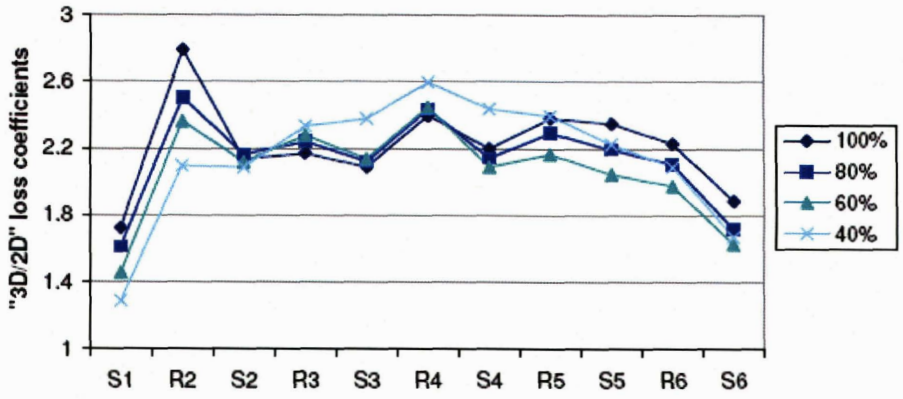


Figure 4.3: "3D/2D" loss coefficients applied to the blade-row 2D losses for different rotor speeds

4.2 Datum Compressor Performance Estimation

Using the mean-line flow analysis coupled with the dynamic-stability model, the datum-compressor map is determined. Figures 4.4 and 4.5 compare the estimated pressure ratio and efficiency maps of the datum compressor to data provided by industry.

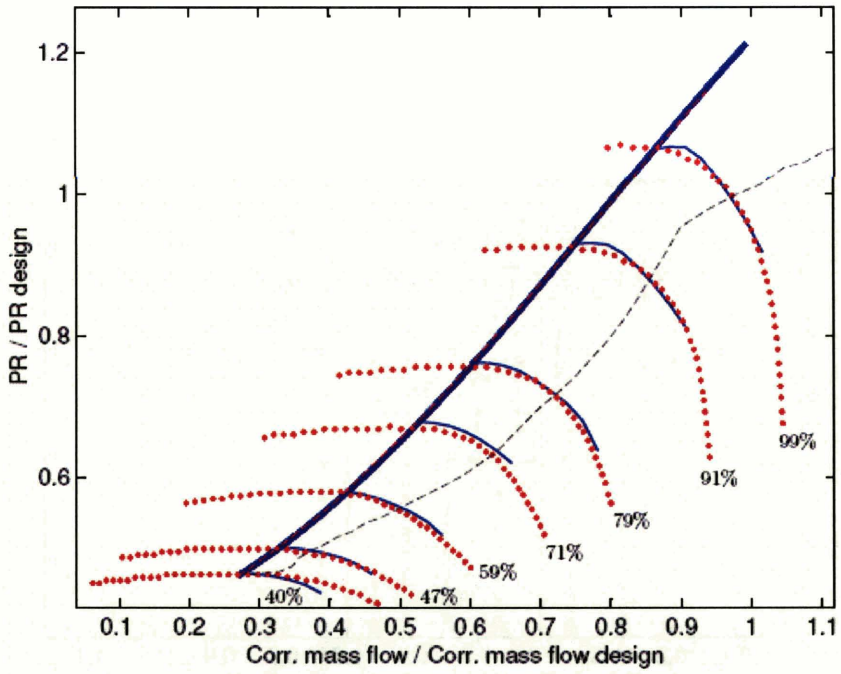


Figure 4.4: Baseline compressor map. The performance estimation is plotted in blue; the performance measurements are plotted in red. The measured operating line is plotted as the black dashed line.

The estimated compressor speed lines, efficiency curves, and surge line compare well with the industry data. The errors are less than 1% in pressure ratio and one point in efficiency as shown in Table 4.1.

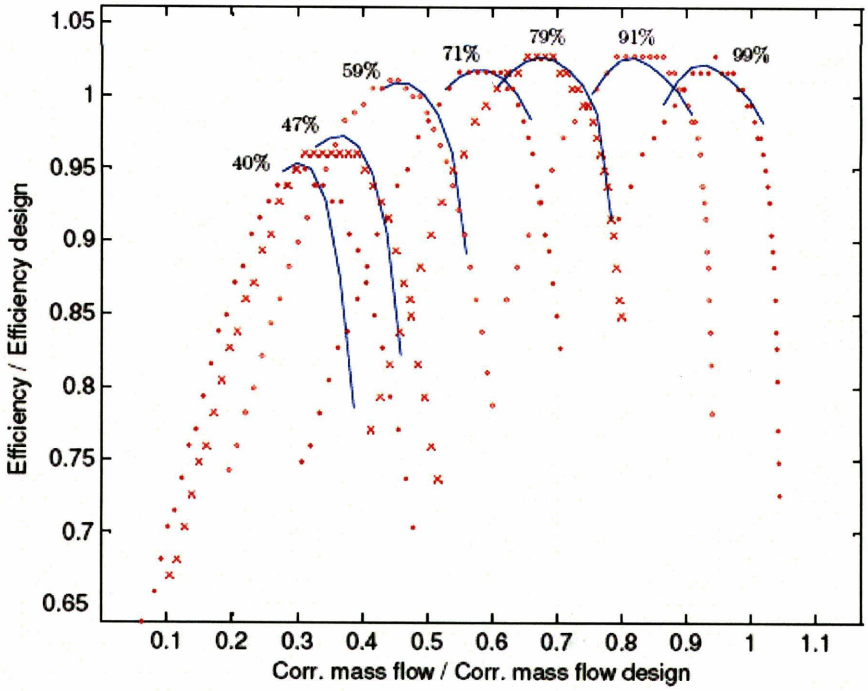


Figure 4.5: Compressor efficiency map. The performance estimation is plotted in blue; the performance measurement is plotted in red.

Speed [%]	$\dot{m}/\dot{m}_{design}$		Estimation	Industry Data	*Error*
99	0.99 (Op)	π/π_{design}	0.992	0.997	0.52%
		η/η_{design}	1.01	1.016	0.6
99	0.87 (Su)	π/π_{design}	1.063	1.065	0.19%
		η/η_{design}	0.993	0.984	0.8
79	0.72 (Op)	π/π_{design}	0.717	0.717	0.11%
		η/η_{design}	1.013	1.011	0.2
79	0.60 (Su)	π/π_{design}	0.752	0.757	0.63%
		η/η_{design}	1.002	1.003	0.1
59	0.50 (Op)	π/π_{design}	0.559	0.555	0.65%
		η/η_{design}	0.997	0.990	0.7
59	0.42 (Su)	π/π_{design}	0.581	0.579	0.28%
		η/η_{design}	1.002	1.005	0.3
40	0.29 (Op)	π/π_{design}	0.466	0.465	0.26%
		η/η_{design}	0.951	0.945	0.5
40	0.27 (Su)	π/π_{design}	0.467	0.465	0.6%
		η/η_{design}	0.946	0.938	0.7

Table 4.1: Compressor-performance comparison between estimation and measurement

These relatively small errors in performance yield errors in the surge margin of less than one point. Table 4.2 shows this comparison for both NASA and industrial surge margin.

Speed [%]		Estimation	Industry Data	Error [points]
99	NASA	16.79	16.68	0.1
	Ind.	19.5	18.88	0.58
79	NASA	20.81	21.15	0.31
	Ind.	24.41	24.73	0.34
59	NASA	18.69	19.07	0.38
	Ind.	17.31	17.75	0.44
40	NASA	5.38	5.75	0.36
	Ind.	2.41	2.76	0.35

Table 4.2: Surge-margin comparison between estimation and measurement

4.3 Datum Compressor Matching

Flow angles and diffusion factors throughout the entire compressor map have been carefully investigated and reviewed by the industry sponsor. The trends and levels of these parameters are consistent with the matching of the datum compressor.

Finally, Figure 4.6 and 4.7 show the blade-row loss buckets of the datum compressor for design speed and flight idle speed respectively. From left to right are plotted the surge point, the design point, and a point on the choke side of the compressor characteristic. For these points, the inlet Mach number differs from one another. Since Mach number affects the loss buckets and only the loss bucket relative to the operating point is plotted, surge points and "choke points" may not lie on the plotted bucket. As can be seen, the low flow angles into Stator 1 and Rotor 2 at low speed yield high levels of loss and steep loss-bucket slopes at surge and operating points.

The Moore-Greitzer model predicts that the growth rate of the flow-field perturbations is proportional to the slope of the non dimensional total-to-static compressor characteristic (Equation 1.3). The steady-state total-to-static pressure rise characteristic can be written:

$$\psi^{TS}(\phi) = \psi_I^{TS}(\phi) - L_R(\phi) - L_S(\phi) \tag{4.3}$$

so

$$\sigma \propto \psi_I^{TS} - \frac{\partial L_R}{\partial \phi} - \frac{\partial L_S}{\partial \phi} \tag{4.4}$$

Therefore, dynamic stability deteriorates with steep negative slopes of the stagnation pressure loss bucket. Stator 1 and Rotor 2 have a significative impact on dynamic stability at low speed.

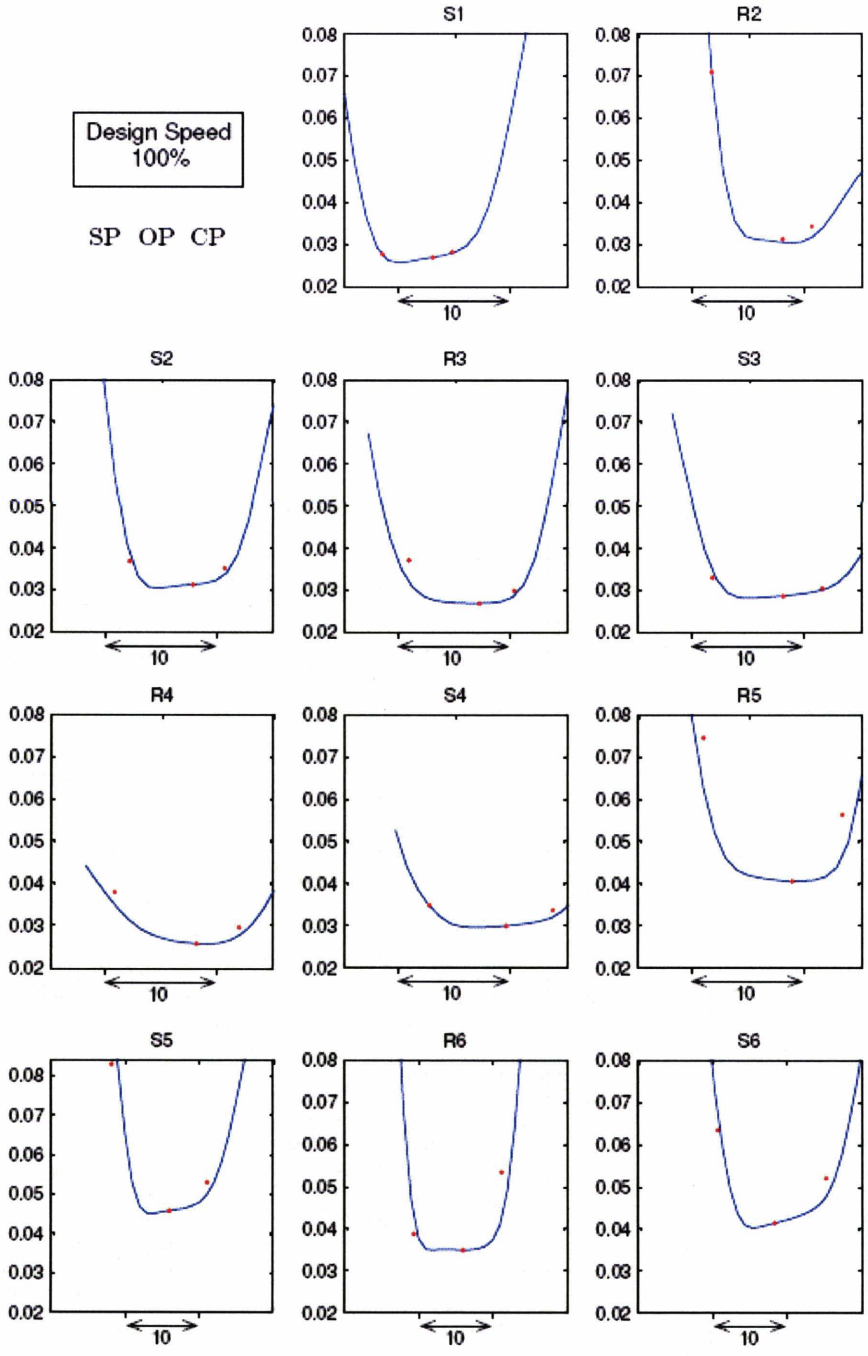


Figure 4.6: Blade-row loss buckets of the datum compressor at design speed. From left to right are plotted the surge point (denoted SP), the design point (denoted OP), and a point on the choke side of the compressor characteristic (denoted CP).

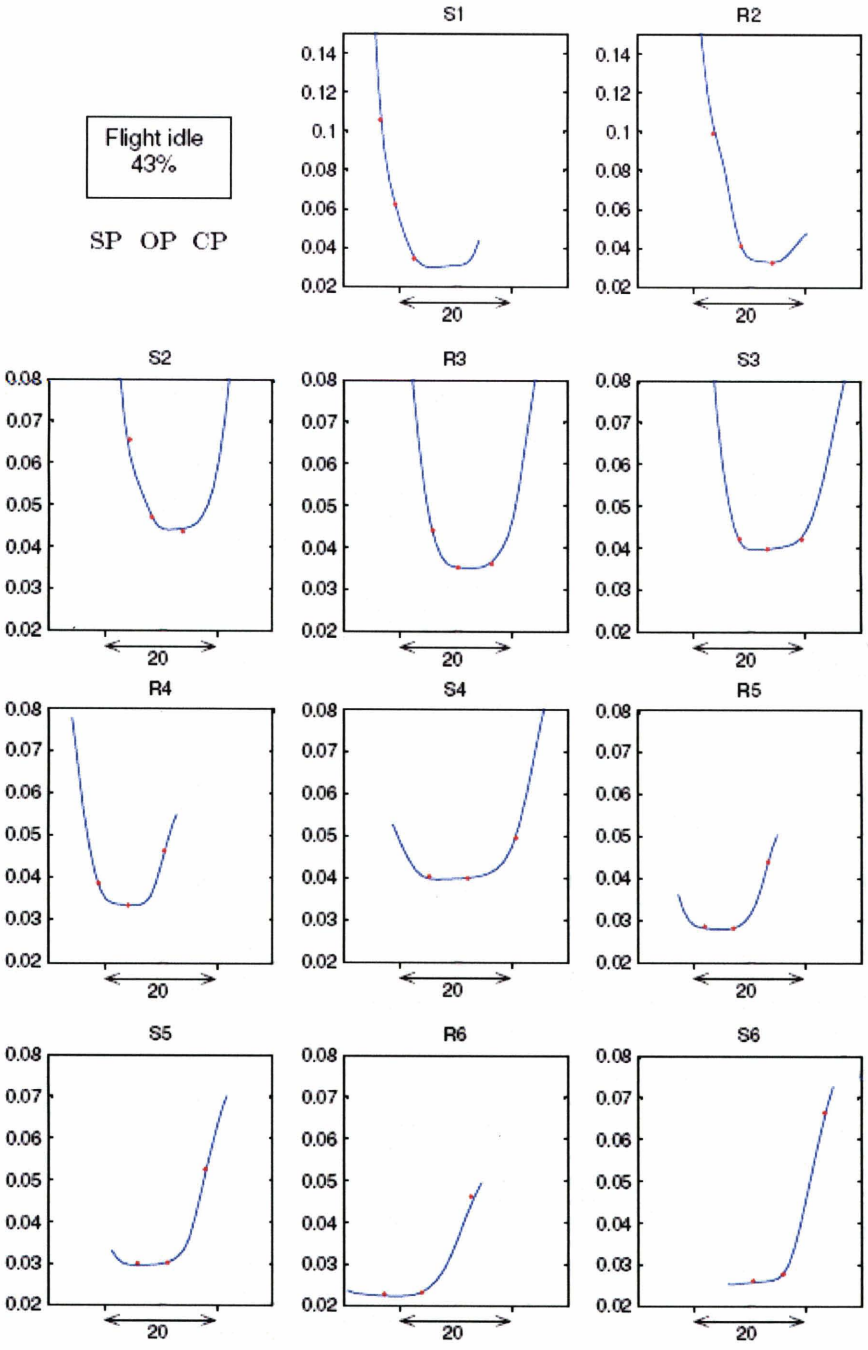


Figure 4.7: Blade-row loss buckets of the datum compressor at flight idle conditions. From left to right are plotted the surge point (denoted SP), the design point (denoted OP), and a point on the choke side of the compressor characteristic (denoted CP).

All the compressor-performance estimation data has been reviewed and assessed by the industry sponsor. The next step of the research is to apply the compressor design optimization framework to the datum compressor.

Chapter 5

Implementation of the Optimization Strategy

5.1 Optimization Strategy

5.1.1 Optimizer Settings

The design methodology developed in this thesis can easily be adapted to the compressor design problem at hand by choosing an adequate objective function. The methodology allows one to optimize the pressure ratio, the efficiency, the stability, or other compressor-performance metrics measured at specific rotor speeds. The general form for the objective function is:

$$Obj = \sum_i \left(w_i \frac{X_i}{X_i^{ini}} \right) \tag{5.1}$$

where X is the metric of choice (e.g., pressure ratio, efficiency, or surge margin). The superscript ^{ini} indicates the baseline value and i indicates the rotor speed at which the metric is evaluated. w is the weighting function in the objective function.

Several optimization strategies are implemented to search for the best compressor-matching solution. The optimization problem in this research is concerned with compressor stability and, more specifically, with the surge margin SM_{ind} at low rotor speed. Hence, one compres-

sor design optimization strategy uses an objective function based on the surge margin SM_{ind} at low speed. But it is also interesting to run optimization cases using the dynamic-stability metric S_d in order to assess the potential benefits of using the suggested new metric in the compressor design process.

The optimization results depend on the initial condition specified by the optimizer. Hence, various compressor design optimizations are conducted using the datum compressor as the initial condition and an altered compressor geometry.

Finally, as previously said, the fan root cannot be altered and the optimizer is not allowed to modify the fan-root geometry.

Stator 6 is also constrained, so the optimizer does not alter the Stator 6 geometry. There are two reasons for this constraint. The first is that the flow out of Stator 6 enters the high-pressure compressor. Therefore, the exit blade angle of Stator 6 cannot be changed. The second is that Stator 6 has little impact on low-speed stability.

5.1.2 Assessment Metrics

The outputs of the optimization framework are systematically examined to assess their validity.

In the blade-performance prediction method, the linear interpolation of blade performance between consecutive points in the database can produce inaccuracies. To assess the accuracy of the optimization result MISES is used to compute the blade performance of the optimized blade geometries. Then the performance of the optimized compressor is calculated using these blade performances instead of using the database.

One must also check if the trends of loss buckets, blade-loading factors, and blade diffusion

factors between the datum compressor and the optimized compressor are consistent with the changes in blade angles.

The purpose of this step in the optimization process is to identify the mechanisms responsible for the compressor-performance improvements. This study permits one to assess the optimization results and to infer some general design implications which might improve the compressor stability.

5.2 Limitations of the Optimization Framework

Investigating the results obtained from the various objective functions and initial conditions helped identify some problems with the database. Some issues could be resolved by refining the database. The limitation here was available computation time.

5.2.1 Interpolation within the Blade Performance Database

To enable variations in blade metal angle during the optimization effort, one needs a database that gathers data for large parameter ranges. As explained in Chapter 3, the parameter increments δ should be kept large in order to reduce the number of points in the database, which in turn reduces the computation time needed to establish the database. Consequently, if one uses large parameter increments, then the interpolated blade performance can yield larger errors.

For example, a 2.5° increment in stagger angle and camber angle in the database led to relative errors of less than 3% in the predicted loss buckets at low rotor speed. However, at high speed and high inlet Mach numbers to the blade rows (Mach numbers above 0.7), MISES encountered some difficulties in converging and the blade row performance was poorly

predicted. Interpolation between these poorly-predicted loss buckets lead to significant errors in blade performance prediction (up to 15% for Rotor 2).

This example suggested to establish a refined database. Hence, a new database with smaller parameter increments of 0.5° or 1° was computed. Consequently, the range of the blade angles was reduced from 10° to 2° or 4°. This refined database was used in the following implementations of the optimization framework.

Using a refined database means that the blade-angle changes may be limited and may reach the constraints specified in the optimization strategy. The alternative to using a refined database is to compute a database with an increased number of data sets (beyond the value of the 25 chosen for this research). This could be achieved using more powerful computing resources.

Also the errors in the results for high rotor speed could be reduced by using a different CFD software such as *Fluent* that has less difficulty in converging for Mach number above 0.8 at high values of incidence angle.

In summary, the main limitations are the computation power and the convergence difficulties encountered by MISES at transonic and highly loaded conditions.

5.2.2 Uncertainty Analysis

It is instructive to measure the effect of one blade-row geometry on the objective function. The low-speed surge margin was evaluated for each point in a blade row database, while the other blade rows remained unaltered. The following example involves Rotor 2. For some of the points plotted on Figure 5.1, constraints on high-speed performance may be exceeded. The figure shows the surge-margin variations at low speed for a variety of Rotor 2

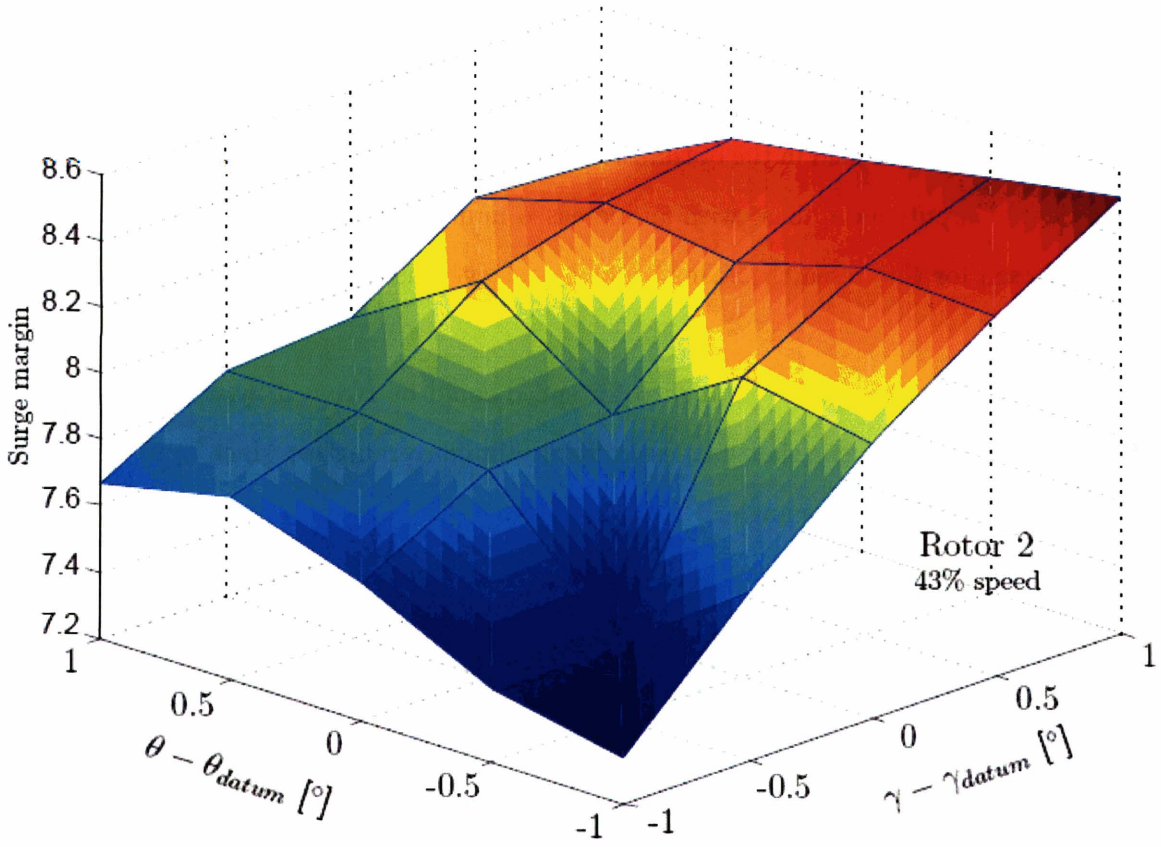


Figure 5.1: The low-speed surge margin versus Rotor 2 geometry (stagger and camber angles). Other blade rows are kept at their baseline geometries.

geometries. The surface displays some local maxima within the geometry domain. For a the datum stagger-angle value, the surge-margin evolution with camber angle is not monotonic as expected; it exhibits variations of 3%. These variations are due to two types of uncertainties. First is the interpolation of stagnation pressure loss between consecutive points (for a given flow angle and Mach number) on the loss bucket. Second is the uncertainty when evaluating the surge margin.

The losses incurred for three different geometries of Rotor 2 at low-speed surge point are compared in Table 5.1:

$\gamma - \gamma_{datum}$ [°]	$\theta - \theta_{datum}$ [°]	Loss [$\times 10^{-2}$]
0	-0.5	8.51
0	0	8.54
0	0.5	8.52

Table 5.1: Blade row loss for three Rotor 2 geometries

The Rotor 2 datum geometry yields the highest loss level, although it was expected to yield a value between the two other values. When MISES is run for the blade geometry, errors in blade performance are about 1%. This error occurs because MISES is not run for the exact operating flow conditions. In this case, loss is interpolated between the loss at the Mach numbers of 0.2 and 0.3 and the flow angles of 43.7° and 44.2°.

The second source of uncertainty stems from evaluating the surge margin. The errors in blade performance lead to an uncertainty on compressor performance, and consequently, to an uncertainty on the surge margin. These uncertainties could be reduced by increasing the number of calculated data sets to generate an entire loss bucket by MISES. This study demonstrates that there is an error of 3% in the surge-margin predictions.

This level of uncertainty is acceptable, but it introduces another challenge for the optimizer. If the topology of the objective function yields too many local minima, the search for a minimum becomes limited because the optimizer can converge towards a minimum close to the initial condition and not explore the entire domain of possible compressor geometries. This can give rise to optimization outputs very close to the datum compressor.

For one of the optimization cases, the compressor geometry was saved at every iteration during the optimization effort in order to determine whether the optimizer explored the entire parameter space. Figure 5.2 shows the evolution of Rotor 2 stagger and camber angles during this optimization. The result shows that the Rotor 2 geometry is perturbed only by very small variations of less than a tenth of a degree. At the end of the optimization, only a limited region in stagger angles and camber angles ([datum value -1° , datum value +1°]) has been explored. The optimizer stops at a local minimum of the objective function near the initial condition.

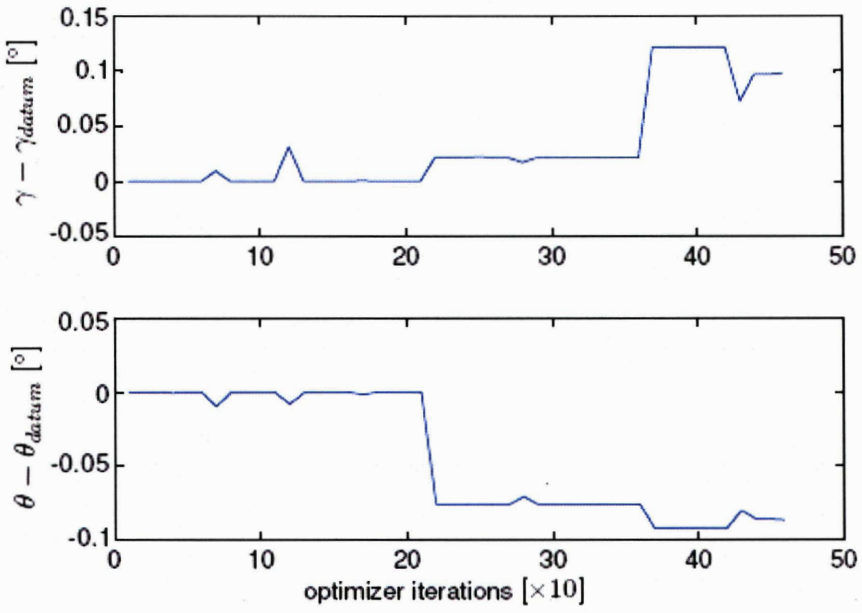


Figure 5.2: Variations of Rotor 2 geometry (stagger and camber angles) during one complete optimization. The full 2° parameter ranges for these angles have not been explored.

In summary, this section shows that the uncertainty in the results is estimated to be 3%. For the optimizations that use a S_d-based objective function, this uncertainty forces the optimizer to converge towards a local minimum of the objective function. Future work to improve the compressor design methodology might involves implementing a search algorithm for a global minimum in the objective function.

Chapter 6

Compressor Design Optimization Results

6.1 Optimization Result Using a SM_{ind} Based Objective Function

This research aims to improve compressor stability at low speed while maintaining high-speed performance. Since the surge margin SM_{ind} is commonly used by industry as the stability metric, this project focuses mainly on applying the optimization framework to the datum compressor using a SM_{ind}-based objective function.

6.1.1 Optimization Strategy

The objective function's weighting function is entirely focused on low-speed stability. The objective function is defined as:

$$Obj = -\frac{SM_{ind\ 43\%}}{SM^{ini}_{ind\ 43\%}} \quad . \tag{6.1}$$

The optimization constraints are summarized in Table 6.1. As discussed previously, the high-speed pressure ratio drop at the operating point is limited to -1%, and the efficiency drop is limited to one point. These constraints apply to operating points at 100% and

108% speed. A constraint concerning high-speed stability is added to these performance constraints. The 100% and 108% speed surge margins are limited to a maximum reduction of two points.

Speed [%]	$(\pi - \pi^{ini})/\pi^{ini}$ [%]	$\eta - \eta^{ini}$ [points]	$SM_{ind} - SM_{ind}^{ini}$ [points]
100	≥ -1	≥ -1	≥ -2
108	≥ -1	≥ -1	≥ -2

Table 6.1: Constraints used in the SM_{ind}-based optimization

6.1.2 Compressor Performance Optimization Results

Table 6.2 summarizes the performance results. An improvement in surge margin SM_{ind} of 1.08 points at low speed is achieved. However, this improvement causes drops in pressure ratio at design speed and climb speed of almost 1%, as well as a drop in efficiency of around 0.3 points. At high speed, stability is improved by two points in surge margin SM_{ind}. Note that the 1% drop in pressure ratio at the operating point yields half (one point) of this stability improvement.

Speed [%]	ΔSM_{ind} [points]	$\Delta\eta$ [points]	$\Delta\pi/\pi_{datum}$ [%]
43	1.08	0.04	-0.02
100	2.19	-0.22	-0.95
108	2.09	-0.34	-0.89

Table 6.2: Comparison between optimized-compressor performance and datum-compressor performance on the operating line for the SM_{ind}-based optimization.

Figures 6.1, 6.2 and 6.3 compare the optimized compressor pressure ratio and efficiency maps to those of the datum compressor. The performance of the optimized compressor is

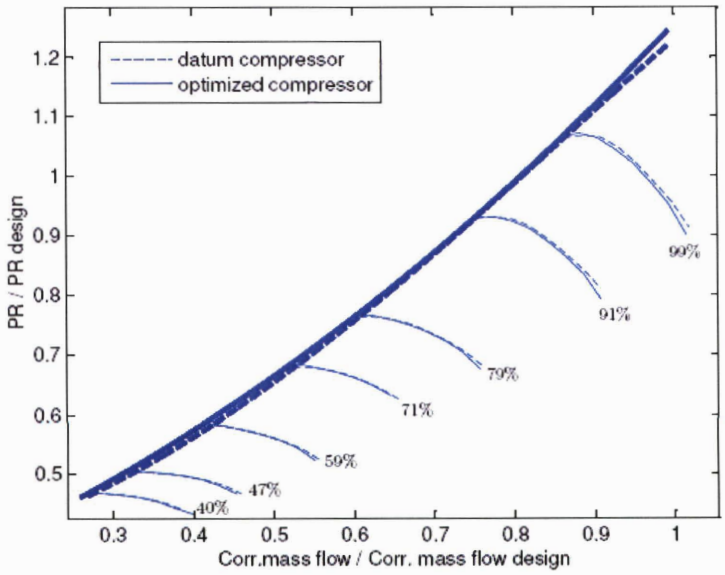


Figure 6.1: Comparison between the optimized-compressor map (SM_{ind} optimization) and the datum-compressor map

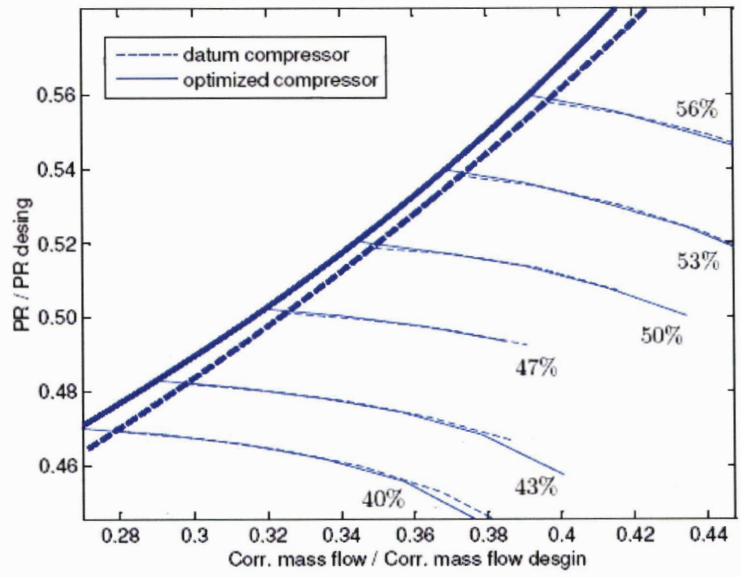


Figure 6.2: Comparison between the optimized-compressor map (SM_{ind} optimization) and the datum-compressor map (low-speed enlarged view)

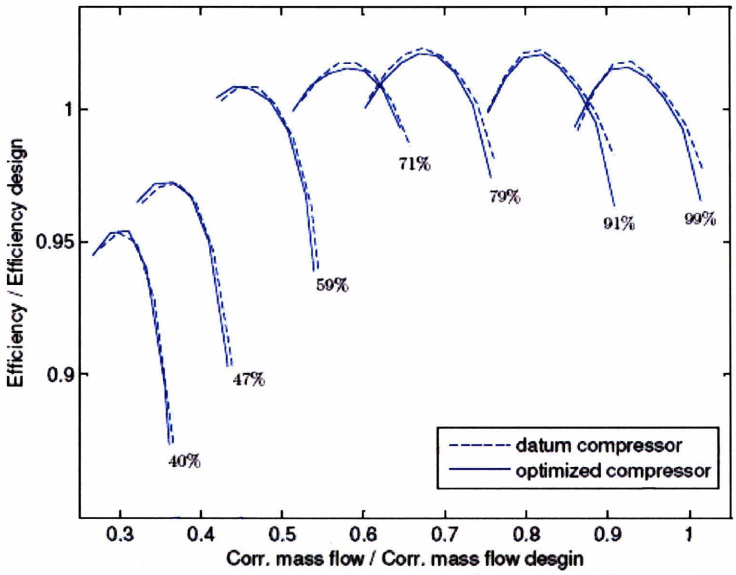


Figure 6.3: Comparison between the optimized-compressor efficiency map (SM_{ind} optimization) and the datum-compressor efficiency map.

plotted as the solid line, and the performance of the datum compressor is plotted as the dashed line. The compressor stability is improved by 14.6% at low speed and by 8.4% at high speed. The high-speed pressure ratio and efficiency characteristics of the optimized compressor are below the datum-compressor characteristics on the operating line (by almost 1% for the pressure ratio and by almost 0.3 points for the efficiency).

Figure 6.4 depicts the blade-angle changes. The stagger angles and camber angles of all of the blade rows are altered. The optimizer increased the stagger and camber angles of most of the blade rows, except for rotor 2 and rotor 6 where the stagger angle decreased.

The next section explains the mechanisms responsible for the improvement in stability.

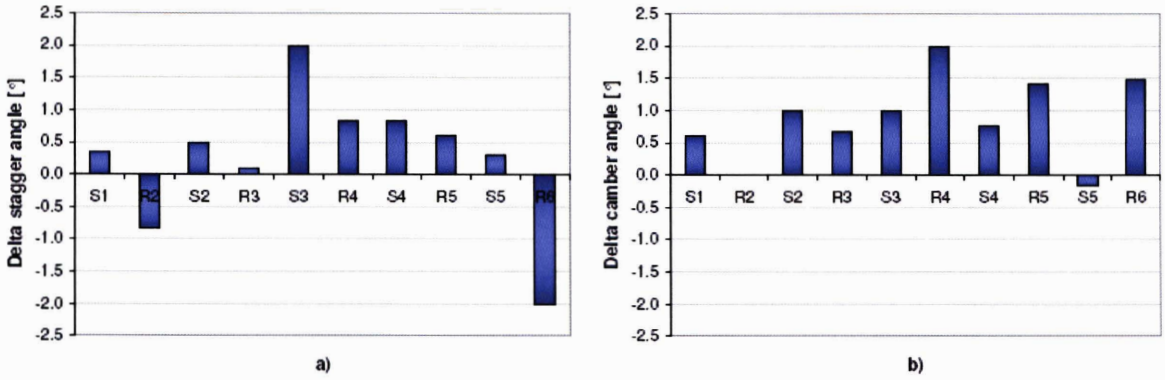


Figure 6.4: a) Variation of blade stagger angles and b) variation of blade camber angles between the optimized-compressor blades and the datum-compressor blades

6.1.3 Analysis of the Results

Loss-Bucket Analysis

The first step is to compare the loss buckets interpolated by the database and the loss buckets computed by MISES for the optimized blade geometries. Figure 6.5 shows the comparison for all the blade rows at the low-speed surge point. The loss buckets of the datum compressor are marked as solid-blue lines. The loss buckets for the optimized compressor interpolated in the database are marked as solid-red lines. And finally, the loss buckets for the optimized compressor computed by MISES are shown as dashed-red lines.

The comparison between loss buckets for the optimized blade geometries yields relative errors of less than 1%. This low error level is achieved by using the refined database discussed in Section 4.1.2.

The impact on the loss bucket of changes in the blade stagger angle and the camber angle is governed by two effects. The first effect is an increase in the overall level of stagnation pressure loss when the stagger or camber angle is increased. The second effect is that the loss buckets are shifted towards smaller flow angles. When the stagger and/or camber angles

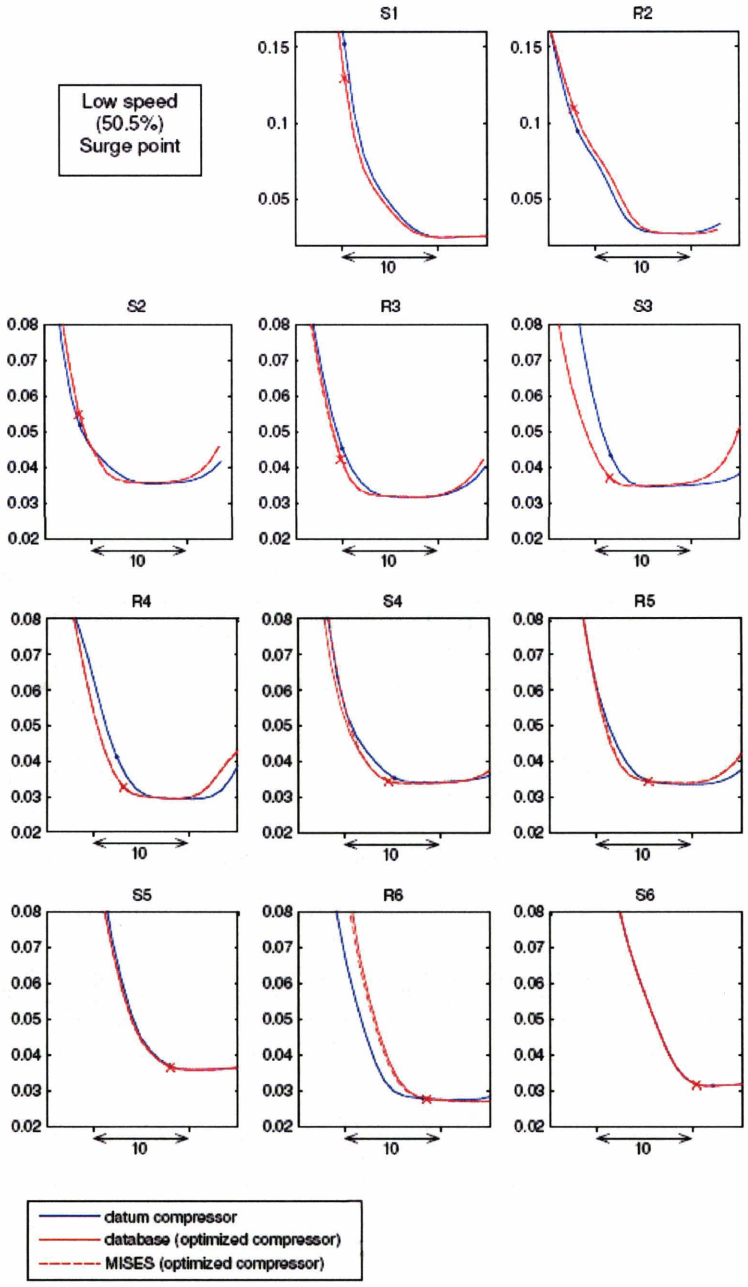


Figure 6.5: SM_{ind}-based optimization: blade-row loss buckets at low speed surge point for the datum compressor (in blue) and the optimized compressor (in red). The solid-red line corresponds to the loss buckets interpolated using the database; the dashed-red line corresponds to loss buckets computed by MISES.

increase, the inlet blade metal angle decreases, and the incidence angle into the blade row for a given flow angle decreases. Generally, the second effect is more dominant, and an increase in the stagger and/or camber angles results in lower loss levels on the surge side of the loss bucket and higher loss levels on the choke side of the loss bucket.

Comparing the optimized compressor and the datum compressor loss buckets shows a trend consistent with the changes in blade angles. The low-speed surge point is on the surge side of the loss bucket. Therefore, if the blade angles increase, as is the case for most of the blade rows, the loss levels for the optimized compressor decrease. The decrease in loss levels and the increase in loss-bucket slopes stabilize the surge point, resulting in an improved surge margin. Equation 4.2 shows that increasing the stagnation pressure loss sensitivity $\partial L/\partial \phi$ reduces the growth rate of the flow field perturbations thus improving dynamic stability.

Table 6.3 and Figure 6.6 summarize the changes in relative flow angles into the blade rows between the datum compressor and the optimized compressor. The table also shows the changes in the inlet blade metal angle due to the modifications in stagger and camber angles. The flow angles and blade metal angles used are defined in Figure 3.2. Changes in the incidence angle into the blade rows are tabulated in the last column.

Blade Row	Δ flow angle [°]	Δ inlet blade metal angle [°]	Δ incidence angle [°]
S1	0	-0.72	-0.72
R2	-0.40	0.83	1.22
S2	-0.18	-1.11	-0.93
R3	-0.18	-0.52	-0.34
S4	-0.12	-2.64	-2.51
R4	0.69	-2.17	-2.86
S4	-0.65	-1.31	-0.67
R5	0.23	-1.47	-1.70
S5	0.07	-0.23	-0.30
R6	0.40	1.18	0.78
S6	-1.73	0	1.73

Table 6.3: Changes in the flow angles, the inlet blade metal angles and the incidence angles between the datum compressor and the optimized compressor for an SM_{ind}-based optimization.

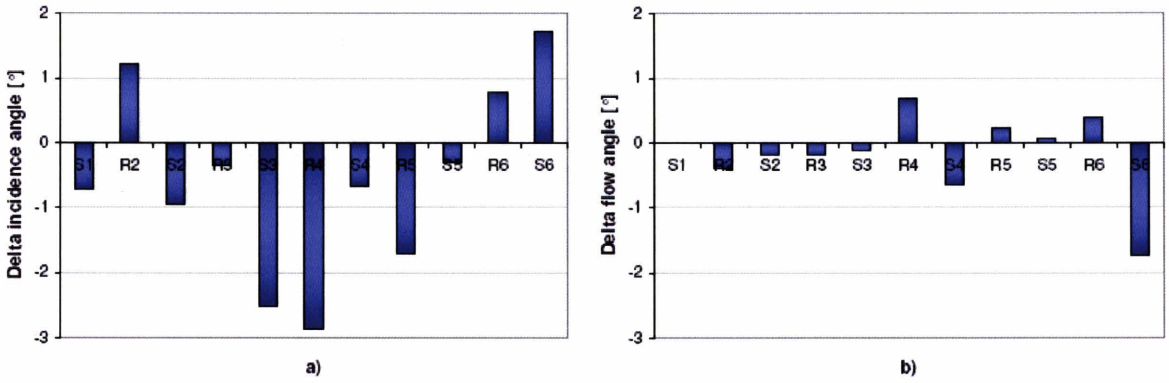


Figure 6.6: Changes in the incidence angles (a) and the flow angles (b) between the datum compressor and the optimized compressor for the SM_{ind}-based optimization.

For all of the blade rows except for Rotor 2 and Rotor 6, the inlet blade angle decreases even if the flow angle is increased, which results in a decrease in the incidence angle. For Stator 6, despite an increase in the incidence angle of almost 2°, there is almost no deterioration in blade performance.

In summary, the optimizer increases the stagger and camber angles for most of the blade rows so that the incidence angles on the blade rows at the low speed surge point will be decreased. The decrease in incidence angles provides a reduction in loss levels and an increase in the loss sensitivity $\partial L/\partial\phi$, which consequently improves stability.

Impact of Changes in Stator 1 Geometry on Compressor Performance

Figure 6.5 depicts the high loss level of Stator 1. As explained in Section 1.1.1, the front end of the compressor, especially stator 1, is responsible for surge at low speed. Therefore, closing the leading edge of stator 1 efficiently increases stability. However, as will be seen later, the high-speed compressor performance is really sensitive to the front stages. Since an

increase in Stator 1 blade angles leads to a higher loss at high-speed operating points, there is a challenging trade-off between low-speed stability and high-speed performance.

A study was conducted to investigate by how much Stator 1 blade angles (both stagger and camber) could be increased before a drop in high-speed pressure ratio of 1% occurred. For this study, the other blade rows were unaltered. Increasing both the stagger and camber angles by 0.7° leads to a drop in design-speed pressure ratio of 0.97%, which caused a 0.49 point improvement in the surge margin SM_{ind} at low speed. In conclusion, this study demonstrates that the improvement in stability at low speed cannot be achieved by changing Stator 1 alone. All blade-row setting angles must also be modified and the compressor must be re-matched.

High-Speed Performance Requirements

The increase in blade angles causes a deterioration of blade-row performance at high speed. Figure 6.7 shows that for all blade rows except for Rotor 2 and Rotor 6, the stagnation-pressure loss increased at design point. This observation is consistent with the changes in blade angles.

High-speed operating pressure ratio is relatively sensitive to Rotor 2 performance. A 0.5° increase in the Rotor 2 stagger angle drops the pressure ratio at the climb speed operating point by another 1%, while improving the low-speed surge margin SM_{ind} by 0.1 point only. Therefore, the optimizer uses Rotor 2 to meet the pressure-ratio requirement and not to improve low-speed stability.

As previously stated, the low-speed stability limit is governed by the front-end of the compressor. Thus, low-speed stability is not as sensitive to the Rotor 6 performance and the Rotor 6 loading is increased to meet the high-speed pressure-ratio requirements. Figure 6.8

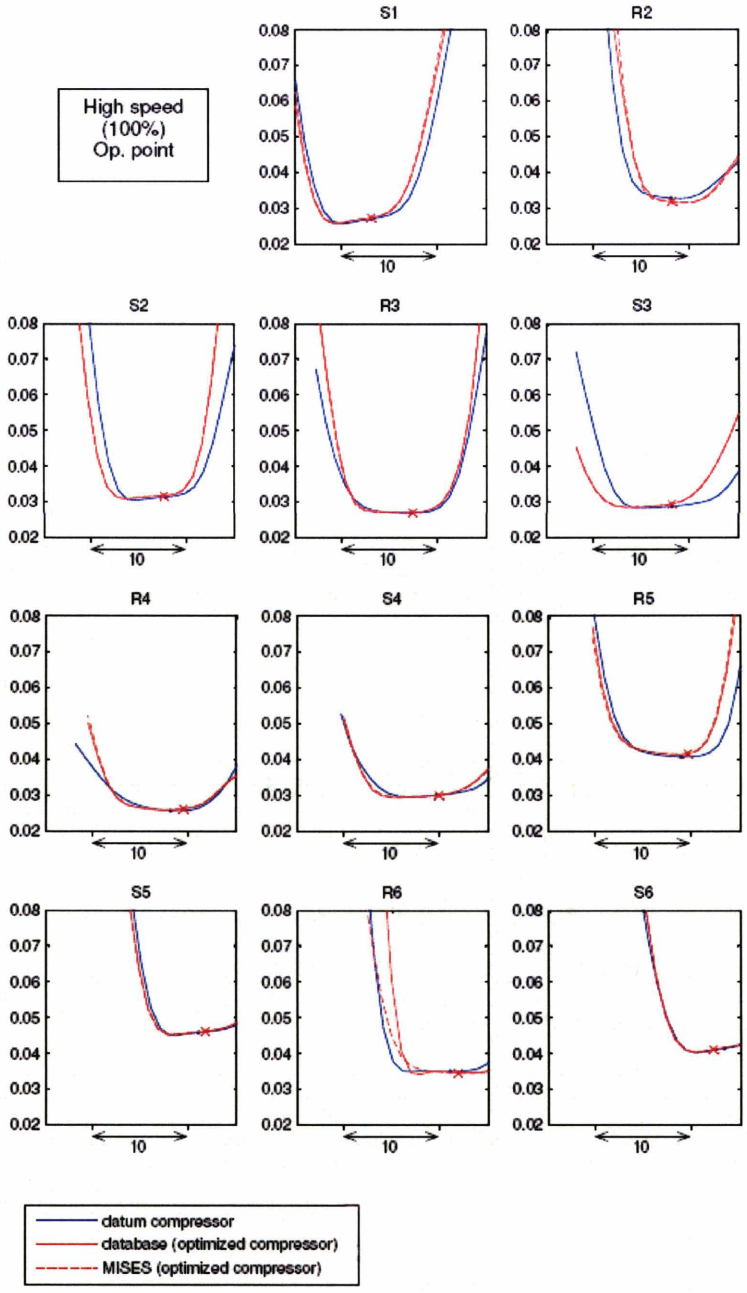


Figure 6.7: Blade-row loss buckets at the design speed operating point for the datum compressor (in blue) and the optimized compressor (in red) (SM_{ind}-based optimization). The solid-red line corresponds to loss buckets from the database; the dashed-red line corresponds to loss buckets MISES provides.

shows the blade loading for all blade rows and the work coefficient for the rotor-blade rows at design conditions.

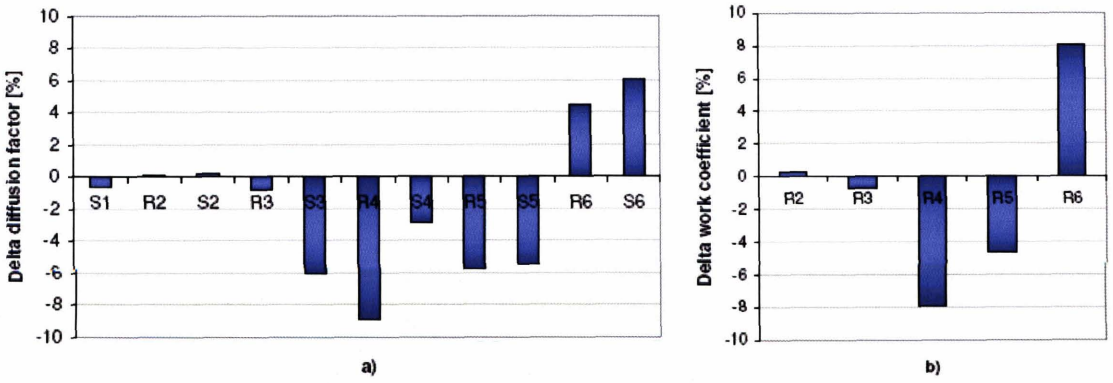


Figure 6.8: a) Variation of the diffusion factor of the blade rows and b) variation of the work coefficient of the rotor blade rows at the design-speed operating point.

The results show that the loading of the front stages is essentially unchanged. The loading in the center of the machine (from Stator 3 to Stator 5) is significantly decreased (by about 5%). And, finally, the loading of the last stage is increased to balance the reduced loading of the center stages. The rotor work coefficients depict the same trend. This improvement in blade performance for Rotor 6 is achieved by decreasing the stagger angle by 2° and increasing the camber angle by 1.4°.

6.1.4 Compressor Design Implications

This compressor design optimization suggests that there are three main changes to the blading of the datum compressor to be considered.

- Improve surge margin SM_{ind} at low speed by increasing the stagger and camber angles of the blade profiles in order to decrease the incidence angles into the blade rows. This decrease in incidence angle results in lower stagnation-pressure loss levels at the low speed surge point and an improvement in dynamic stability. An increase in the stagger and camber angles can be applied to Stator 1. Since the loss bucket on the stall side is steep, a small change in the incidence angle of 0.7° generates a 15% drop in loss. However, too large an increase in the stagger and camber angles (0.7° for each angle) may cause the constraints on high-speed pressure ratio to be exceeded.

- An increase in the blade angles causes the blade performance and blade loading at high speed operating point to deteriorate. Therefore, the loading of several blade rows must be increased to meet the high-speed pressure ratio and efficiency requirements. Since the high-speed pressure ratio is relatively sensitive to Rotor 2, Rotor 2 loading should be increased by reducing the Rotor 2 stagger angle.

- The last stage has relatively little impact on the low-speed stability. And the stage loading also is increased to ensure the pressure-ratio requirements at high speed. The stagger and camber angles of Rotor 6 are decreased and increased respectively in order to improve the Rotor 6 loading and work coefficients and to balance the reduced loading of the center stages. Finally, an increase in the Rotor 6 stagger and camber angles leads to a decrease in the flow angle into Stator 6 and improves Stator 6 loading, as well.

6.1.5 Discussion of Results

The results were discussed with the industry sponsor, who expressed two major concerns. The increase in the Rotor 2 incidence angle presents some risks since the stability limit at low speed is governed by the front stages of the compressor. The industry sponsor suggested

instead that the Rotor 2 stagger angle be increased and the incidence angle be reduced. The second suggestion concerns Rotor 6. Since Rotor 6 is located in a "goose-neck" type gas path, an increase in the Rotor 6 loading could lead to an increase in secondary flows at the hub, which can lead to endwall flow reversal. This effect is not taken into account in this research, since the endwall flow is not modeled. Therefore, the loading of Rotor 6 should be kept at its datum value.

In conclusion, given the deterioration in the high-speed pressure ratio and efficiency, and the risks listed above, the datum compressor is suggested to be optimally matched.

6.2 Optimization Result Using an S_d Based Objective Function

The research also aims to investigate the potential benefits in operability that could be achieved if the compressor design is optimized using the dynamic-stability metric, S_d. The optimization framework is thus applied to the datum compressor using an objective function based on S_d. Unfortunately, the optimizer encountered some convergence issues and did not provide instructive results. As discussed in Section 4.2.2, the result briefly presented here is close to the datum compressor.

6.2.1 Setup of the Optimizer

The objective function used during this optimization differs from the objective function

previously used in that it is based on S_d instead of SM_{ind}.

$$Obj = -\frac{S_{d\ 43\%}}{S_{d\ 43\%}{}^{ini}} \tag{6.2}$$

The optimization constraints used for the high-speed performance are the same as before. Only the constraint concerning high-speed stability is modified and related to S_d instead of SM_{ind}. The 100% and 108% speed values of S_d are limited to a maximum reduction of 5%.

Speed [%]	$(\pi - \pi^{ini})/\pi^{ini}$ [%]	$\eta - \eta^{ini}$ [points]	$(S_d - S_d^{ini})/S_d^{ini}$ [%]
100	≥ -1	≥ -1	≥ -5
108	≥ -1	≥ -1	≥ -5

Table 6.4: Constraints used in the S_d-based compressor design optimization.

For this case, the initial condition used in the optimization was not set to the datum compressor, but to a compressor geometry with a modified Stator 1 blade row ($\gamma = \gamma^{ini} + 0.5°$ and $\theta = \theta^{ini} + 0.5°$).

6.2.2 Preliminary Results

As mentioned earlier, the resulting compressor is close to the datum compressor. Table 6.5 shows that the optimizer did not alter the compressor geometry of the initial setting and stopped at a local minimum of the objective function.

The optimization using S_d in the objective function is sensitive to topology of the objective function. If the topology yields too many locals minima, the optimizer can converge towards a minimum close to the initial setting and does not explore the entire domain of

	Rotor		Stator	
Stage	γ [°]	θ [°]	γ [°]	θ [°]
1	—	—	0.5	0.498
2	0.01	0	0	0.01
3	-0.01	0.01	-0.01	0.01
4	-0.02	-0.01	-0.01	0
5	0	0.01	0.01	0.01
6	0.02	0.01	—	—

Table 6.5: S_d-based optimization: changes in blade angles between the resulting compressor and the datum compressor. The changes are negligible.

possible compressor geometries. This application of the optimization framework requires a more global search for minima. Also, reducing the uncertainty in evaluating the compressor stability by increasing the number of points computed for a entire loss bucket could lead to better results.

The comparison between the performance of the resulting compressor and the datum compressor is summarized in Table 6.6. The improvement in low-speed S_d is +7.3%, and the corresponding improvement in the low-speed surge margin SM_{ind} is 0.32 points. These improvement are mainly due to an increase in the Stator 1 blade angles.

Speed [%]	ΔSM_{ind} [points]	$\Delta\eta$ [points]	$\Delta\pi/\pi_{datum}$ [%]	$\Delta S_d/S_d^{datum}$ [%]
43	0.32	0.2	0.02	7.3
100	0.61	0.07	0.37	-1.83
108	0.71	0.11	0.64	1.69

Table 6.6: S_d-based optimization: comparison between output-compressor performance and datum-compressor performance on the operating line.

The compressor pressure ratio and efficiency maps do not reveal a significant improvement. However, it is worth noting that, as shown in Figure 6.9, there is some improvement in surge margin at 43% speed. For higher speeds, the surge line of the output compressor merges with the surge line of the datum compressor.

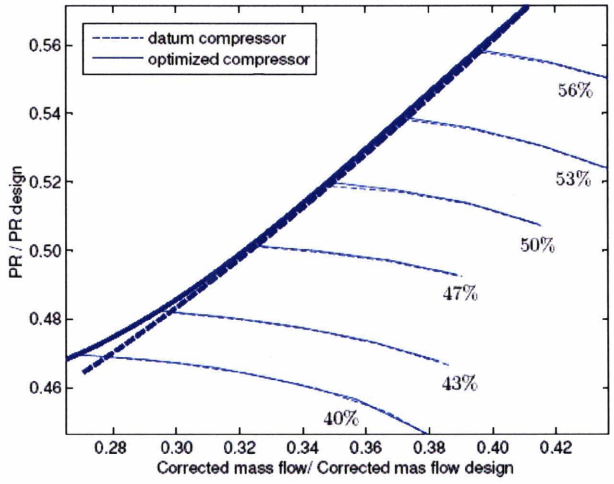


Figure 6.9: S_d-based optimization: comparison between the resulting-compressor map and datum-compressor map (low-speed enlarged view).

6.2.3 Discussion of Results

During this optimization strategy, the optimizer converged towards a local minimum of the objective function very close to the initial setting. The optimizer did not explore the entire domain of the compressor settings. Thus, a search algorithm for a global minimum of the objective function must be developed in order to improve the compressor design optimization framework and to explore the potential of an S_d-based optimization.

However, this simple result demonstrates that a large improvement in the dynamic-stability metric S_d at low speed does not necessary imply a large improvement in the surge margin SM_{ind}. S_d is concerned with the dynamic stability on the 43% speed compressor characteristic while SM_{ind} is concerned with the compressor stability at a rotor speed of around 50% at a constant corrected mass flow.

Chapter 7

Summary and Conclusions

7.1 Compressor Performance Estimation

The compressor design optimization methodology developed in this thesis aims to improve the performance and stability of the datum compressor. Since the the optimization results rely on the accuracy of the compressor performance and stability prediction method, this method must accurately estimate the performance and stability of the datum compressor. Therefore, the first milestone of this research was to develop a mean-line flow analysis capable of adequately estimating the datum performance and stability.

The datum compressor consists of a fan root and a 5–and–1/2-stage LPC. The fan-root geometry cannot be altered during the optimization, and a simple model is developed to estimate the fan-root performance. Performance estimation of the 5–and–1/2-stage LPC involves a mean-line code that uses an endwall loss correlation and an off-design performance model. The models developed are simple and enable an accurate estimation of the datum-compressor performance.

A previously developed dynamic-stability compressor model is coupled with this mean-flow analysis to estimate the compressor's stability throughout the entire compressor map. The dynamic-stability model is used to estimate the compressor stall line.

The analysis shows that the datum compressor performance and stability estimations compare well with the performance and stability data provided by industry. To assess the

performance and stability prediction method, the matching of the compressor is carefully investigated, and reviewed by the industry sponsor.

7.2 Blade Performance Prediction

During the compressor design optimization effort, the optimizer alters the stagger angle and the camber angle of the blade rows. A blade-profile parametrization is developed to explore a range of possible geometries. It is important that the blade-profile parametrization capture the datum blade profiles. The profile description involves seven parameters, such as blade stagger and camber angles, and a thickness distribution based on Bezier splines. Comparing the blade performance of the datum profiles and the parameterized profiles yields errors in stagnation pressure loss of less than 1%.

In the search for an optimum compressor design, blade geometries are modified and the associated blade performances are used to evaluate the objective function. A real time numerical simulation using MISES is too costly to run online with the optimizer. One alternative is to create a database that gathers the blade performance data required by the optimizer. A sensitivity study of blade performance to blade-angle changes shows that the ranges of the stagger and camber angles can be limited to a 1° or 2° change from the datum value, depending on the blade row. MISES is used to compute the blade-row performance of 25 different blade geometries for a range of blade angles.

The blade stagnation pressure loss and deviation angle of any selected geometry is estimated by a linear interpolation in stagger and camber angles. This blade-performance estimation method yields relative errors of 1% in stagnation pressure loss and allows a significant reduction in computation time.

However, the errors in the blade-performance prediction method increase the number of local minima in the objective function's topology and cause the optimizer algorithm to fail when it uses an S_d-based objective function. To reduce these errors, especially at high rotor speed, it is suggested to use a CFD software that converges at transonic and highly loaded conditions.

7.3 Compressor Design Optimization Results

The compressor optimization strategy yields an improvement of 1.08 points in the surge margin SM_{ind} at flight idle condition while also meeting the performance requirements at design speed. This improvement was achieved by re-matching the compressor. Most of the blade angles increased, resulting in reduced incidence angles into the blade row. This increase in blade angles stabilizes the surge point at low speed but reduces blade performance at high power. For Rotor 2 and Rotor 6, the blade loading increased in order to balance the reduction in loading of the other stages and to meet the performance requirements at design and climb speed.

However, the optimized geometry with improved low-speed surge margin involves some risks. For instance, an increase in the loading near the hub of Rotor 6 runs the risk of endwall flow separation due to stronger secondary flows.

The best results is a 14.8% improvement in the flight idle surge margin, but the re-matching of the compressor and the associated increase in the rotor loading of the second stage entail high-risk design modifications. This suggests that, given these design limitations, the best matching is achieved by the datum configuration. In summary, the thesis demonstrates that the developed compressor design optimization methodology is applicable to industry-strength design problems, and the framework is shown to have the potential to

investigate compressor designs for optimum matching.

7.4 Recommendation for Future Work

This research suggests that the datum compressor design cannot be further improved using the compressor design optimization framework with an SM_{ind}-based objective function.

Due to time constraints, the S_d-based optimization strategy could not be fully explored, and the preliminary results suggest that further work is required. One possible way to improved the optimizer would be to combine the existing optimization algorithm with a so called "Shot-Gun" optimizer as developed by Spakovszky [16]. The "Shot-Gun" optimizer evaluates the objective function at a few points in the parameter domain in order to find a global minimum. This methodology could be used to ensure that the entire design space is explored.

Further improvements could also be achieved using alternative CFD flow solvers such as *Fluent* to predict blade-row performance under a larger range of flow conditions — especially at transonic and highly loaded conditions. Using an alternative CFD flow solver could improve the accuracy of the objective function evaluation and lead to better results.

Bibliography

[1] CASTIELLA RUIZ DE VELASCO, J.C., *A Novel Design Methodology For Enhanced Compressor Performance Based on a Dynamic Stability Metric*, Masters Thesis, Department of Aeronautics and Astronautics, Massachusetts Institute of Technology, 2005.

[2] CUMPSTY, N., *Compressor Aerodynamics*, Addison-Wesley Publishing Company, 1998.

[3] DORCA LUQUE, J., *Application of an Energy-Like Metric for Axial Compressor Design*, Masters Thesis, Department of Aeronautics and Astronautics, Massachusetts Institute of Technology, 2003.

[4] DRELA, M., YOUNGREN, H., *A User Guide to Mises 2.53.* MIT, Computational Aerospace Sciences Laboratory, 1998.

[5] EMMONS, H.W., *Compressor Stall and Surge Propagation*, Trans. ASME, 1955, Vol 77, pp. 455-469.

[6] EPSTEIN, A.H., FFOWCS WILLIAMS, J.E., GREITZER, E.M., *Active Suppression of Aerodynamic Instabilities in Turbomachines*, AIAA J. Propulsion and Power, Vol 5, pp. 204-211.

[7] GARNIER, V.H., EPSTEIN, A.H., GREITZER, E.M., *Rotating Waves as a Stall Inception Indication in Axial Compressors*, ASME J. Turbomachinery, 1991, Vol 113, pp. 290-301.

[8] GREITZER, E.M., *Stability of Pumping Systems The 1980 Freeman Scholar Lecture*, Journal of Fluids Engineering (Jun. 1981), Vol 103, pp. 193-240.

[9] KERREBROCK, J.L., *Aircraft Engines and Gas Turbines*, 2nd ed. The MIT Press, Cambridge, Massachusetts, 1992.

[10] LONGLEY, J., *A Review of Nonsteady Flow Models for Compressor Stability*, ASME J. Turbomachinery, 1994, pp. 202-215.

[11] MCDOUGALL, N.M., CUMPSTY, N., HYNES, T.P., *Stall Inception in Axial Compressors*, ASME J. Turbomachinery, 1990, Vol 112, pp. 116-125.

[12] MOORE, F., *A Theory of Rotating Stall Multistage Axial Compressors: Part 1-3*,

ASME J. of Eng. Power, 1984, Vol 106, pp. 313-336.

[13] MOORE, F., and GREITZER, E.M., *A Theory of Post-Stall Transients in Axial Compressors: Part I Development of the Equations*, ASME J. of Engineering for Gas Turbines and Power, 1986, Vol 108, pp. 68-76.

[14] PADUANO, J.D., GREITZER, E.M., EPSTEIN, A.H., *Compression System Stability and Active Control*, Annu. Rev. Fluid Mech, 2001, 33:491-517.

[15] PERROT, V., *A Design Optimization Framework for Enhanced Compressor Stability Using Dynamic System* , Masters Thesis, Department of Aeronautics and Astronautics, Massachusetts Institute of Technology, 2003.

[16] SPAKOVSZKY, Z., *Applications of Axial and Radial Compressor Dynamic System Modeling*, PhD Thesis, Department of Aeronautics and Astronautics, Massachusetts Institute of Technology, 2000.